UNIVERSITY OF PÉCS

Doctoral School of Physics
Laser Physics, Nonlinear Optics, and Spectroscopy Program

Investigation of Scalable Concepts for Intense Terahertz Pulse Generation

PhD thesis

Priyo Syamsul Nugraha

Supervisor:
Dr. József András Fülöp
University of Pécs

PÉCS, 2019

Contents

List of Figures

Abbreviations

2PA	:	Two-photon absorption
3PA	:	Three-photon absorption
4PA	:	Four-photon absorption
CG	:	Contact grating
CLN	:	Congruent lithium niobate
CW	:	Continuous wave
DFG	:	Difference frequency generation
EOS	:	Electro optic sampling
FCA	:	Free-carier absorption
FWHM	:	Full width at half maximum
LN	:	Lithium niobate
MPA	:	Multiphoton absorption
NIR	:	Near-infrared
NLES	:	Nonlinear echelon slab
OPA	:	Optical parametric amplifier
OR	:	Optical rectification
PPLN	:	Periodically poled lithium niobate
SHG	:	Second-harmonic generation
SLN	:	Stoichiometric lithium niobate
TO	:	Transverse optical
TPFP	:	Tilted pulse front pumping

1. INTRODUCTION

Terahertz (THz) radiation is a band of electromagnetic radiation, which is located between microwaves and infrared radiation (Figure 1-1), and it shares some properties with each of these. THz radiation, unless very intense, is non-ionizing. The THz band remained unexplored for a long time due to the lack of useful sources and detectors [1]. Therefore, this spectral range was often called the THz gap. Since the mid-70's, advances in electronics and photonics have provided new materials and devices that made the THz gap accessible and triggered rapid progress in both fundamental research and application.

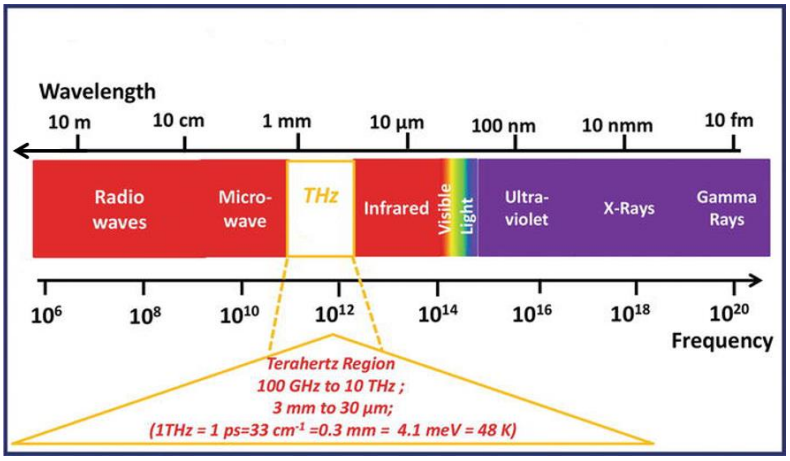

Figure 1-1. THz band in the electromagnetic spectrum [2]

Science and technologies based on THz frequency electromagnetic radiation have developed rapidly over the last 30 years, to the extent that it now touches many areas from fundamental science to real applications [3]. Today, a wide range of possible implementations of THz technology in various fields, such as imaging, sensing, quality control, wireless communication, and basic science, is stimulating enormous attention [4-8]. THz radiation can pass through a wide variety of non-conducting materials such as clothing, paper, cardboard, wood, plastic, and ceramic. Due to its longer wavelength, images made using THz waves have lower resolution than images created with optical or X-rays and need to be enhanced.

In the THz band, based on device operation modes, two major technological families can be distinguished: continuous-wave [9-11] and pulsed operation. Continuous-wave systems typically operate at a single frequency. Therefore, they are narrowband and can have a high spectral resolution. Because of this, continuous-wave systems are useful for gas-phase spectroscopy [12], telecommunication [13], and non-destructive inspection [14]. Pulsed or time-domain THz systems are base on the generation and detection of transient electromagnetic fields with typical durations of a few picoseconds. A short pulse is composed of many

frequencies, which can be accessed by the Fourier transform of the temporal waveform. As opposed to continuous-wave systems, pulsed systems are broadband in nature, and emission is not continuous. Therefore, pulsed systems are ideal for spectroscopic applications [15,16] and the study of ultrafast phenomena. Pulsed THz systems are typically driven by picosecond or femtosecond pulsed lasers and the development of suitable photonics technologies also triggered the evolution of related THz technologies. Source development is a rapidly developing area of THz research.

The linear absorption coefficient and the refractive index of various materials in the THz range can be measured by linear (time-domain) spectroscopy. In contrast to monitoring the linear response with weak pulses, strong-field THz pulses with electric field strengths of about 100 kV/cm or more can induce changes in materials. These changes can be investigated by nonlinear spectroscopic methods, such as THz pump—THz probe measurements. For example, nonequilibrium dynamics in superconductors, multiferroics, and magnetic materials could be studied in this way [17]. At still higher THz field strengths, the effective manipulation of charged particles – primarily electron (beam) acceleration, undulation, deflection, spatial, and temporal focusing – became available [18].

The development of intense pulsed THz sources is the main subject of the present work. The aim was to create simple, easily available sources with high intensity and controllable pulse parameters. Novel THz sources based on lithium niobate (LN) and semiconductor nonlinear optical crystals were investigated both by numerical simulations and experimental studies.

The dissertation is structured as follows. Next, Chapter 2 describes the background of THz sources based on nonlinear optical crystals, THz pulse characterization, and multiphoton absorption. The brief Chapter 3 sets the scientific goals. In Chapter 4, the results of the work are discussed in three topics. First, the experimental demonstration of a novel LN THz source is presented, which can be scaled to high THz pulse energies and field strengths by providing a THz beam with uniform waveform and excellent focusability. Second, the expected performance of semiconductor-based multicycle THz sources is investigated by numerical simulations. Third, the measurement of intensity-dependent effective multiphoton absorption coefficients in semiconductors is shown. Chapter 5 contains the thesis statements. Chapter 7 gives a brief summary and Chapter 8 the publication list of the author.

2. BACKGROUND

2.1. THz generation by second-order nonlinear optical processes

In linear optics, the polarization induced in a medium by an optical field is proportional to the electric field. In nonlinear optics, the interaction between the optical field and the medium depends on the field strength in a nonlinear manner. Nonlinear polarization can easily be induced by an intense short laser pulse [19].

Technological advances in optics and electronics resulted in a great variety of different THz sources (Figure 2-1). Many of these rely on nonlinear optical materials, in which the incident electromagnetic wave undergoes nonlinear frequency conversion. Optical rectification and difference-frequency generation are second-order nonlinear optical processes in which a THz photon at a frequency ω_T is created by the interaction of two optical photons at frequencies ω_1 and ω_2 within the nonlinear crystal [20].

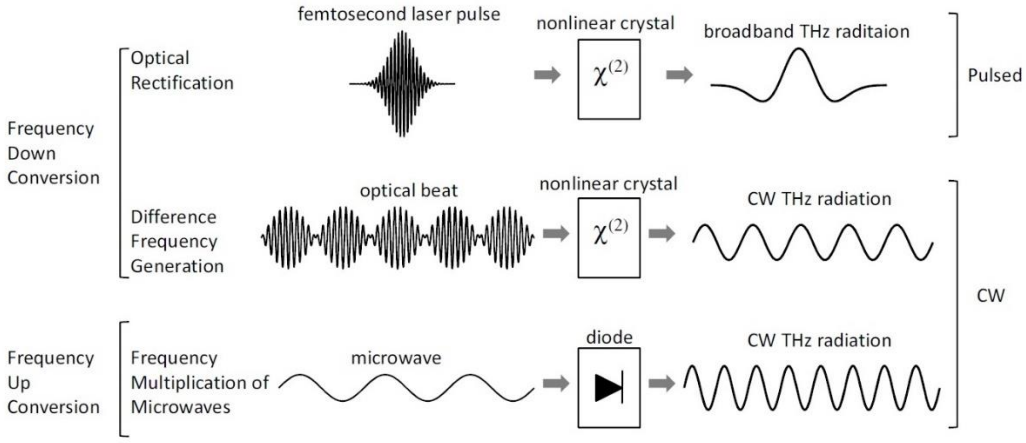

Figure 2-1. THz generation in nonlinear crystals [20].

In 1965, using a ruby laser, Zernike and Berman performed the first THz generation experiment based on difference-frequency mixing in a quartz nonlinear optical crystal, placed inside the laser cavity [21]. Later, tunable THz-frequency output was also demonstrated by difference-frequency generation in other nonlinear optical materials. Both collinear and noncollinear phase matching were used to generate broadly tunable 0.6-5.7 THz output in LN [22]. Collinear phase-matching was achieved in the birefringent crystals $ZnGeP_2$ [23,24] and GaSe [25], and noncollinear phase matching in the cubic zinc-blende type crystals GaAs [26,27] and GaP [28]. In GaP, collinear phase matching was also demonstrated [29].

Broadly tunable (0.3–3.0 THz) quasimonochromatic THz radiation can be produced through THz-wave parametric oscillation in bulk LN crystal with a single fixed-frequency optical pump. In this case, phase matching can be achieved by noncollinear three-wave interaction. The pump and the (resonating) signal waves are in the near-infrared, and the outcoupled nonresonant wave is in the THz range [30,31]

Broadband THz output can be produced in a nonlinear optical medium via difference-frequency mixing between pairs of Fourier components of the same optical pulse. This case is usually referred to as optical rectification. First demonstrations of this method used picosecond pulses and $LiNbO_3$ [32,33], ZnTe, ZnSe, CdS, and quartz [32] crystals. Later, it was extended to femtosecond laser pulses [34], which enabled to generate much broader bandwidths in the THz region [35]. Typically, thin (~1 mm or less) electro-optic crystals were used, because of constraints associated with the mismatch between optical group and THz phase velocities, as well as the strong THz absorption in conventionally applied crystals ($LiNbO_3$, ZnTe). Optical rectification was also demonstrated in zinc-blende type GaAs [36,37] and GaP [38] crystals, which have much smaller THz absorption. Optical rectification will be discussed in more detail in Section 2.2.

THz sources based on second-order nonlinear optical effects, in particular, difference-frequency generation, optical rectification, and optical parametric oscillation, are very appealing because they can utilize diode-pumped laser technology. Another advantage of these techniques is their power scalability. Unlike photo-mixers and dipole photoconductive antennas [39], nonlinear optical sources do not suffer from a saturation of THz output power. The power output typically shows quadratic dependence on the pump power up to high power levels [40].

2.2. THz sources based on optical rectification

Optical rectification of ultrashort laser pulse can be considered as a result of difference-frequency mixing among the spectral components contained within the short pulse bandwidth (see also Section 2.1). For phase-matched condition (see below), the efficiency of THz generation by long plane-wave pulses can be described by the following equation [41]:

$$\eta_{THz} = \frac{2\omega^2 d_{eff}^2 L^2 I}{\varepsilon_0 n_{NIR}^2 n_{THz} c^3} exp\left[-\alpha_{THz} {}^{L}/_{2}\right] \frac{sinh^2\left[\alpha_{THz}\left({}^{L}/_{4}\right)\right]}{\left[\alpha_{THz}\left({}^{L}/_{4}\right)\right]^2}. \quad (1)$$

Eq. (1) is valid in the absence of pump absorption or depletion, and it takes into account THz absorption. Here, ω is the angular difference (THz) frequency, d_{eff} the effective nonlinear coefficient, I the intensity of the near-infrared light, ε_0 the vacuum permittivity, c the velocity of light in vacuum, L the length of the nonlinear crystal, α_{THz} the intensity absorption coefficient for the THz radiation, and n_{NIR} and n_{THz} the refraction indices in the NIR and THz range, respectively. The effective nonlinear coefficient d_{eff} can be calculated using the clamped electro-optic coefficients r and the NIR refractive index values n_{NIR} as follows [42];

$$d_{eff} = -n_{NIR}^4 \, r/4. \tag{2}$$

For efficiently generating THz frequency, the phase-matching condition requires the group velocity of the laser pump pulse to be equal to the phase velocity of the THz radiation [43].

$$v_{NIR}^{gr} = v_{THz} \tag{3}$$

Table 1 compiles the optical group indices at two common pump wavelengths, the THz refractive indices and absorption coefficients at 1 THz frequency for a few selected materials suitable for optical rectification.:

$$n_{NIR}^{gr} = n_{THz} \tag{4}$$

Table 1. Properties of nonlinear material suitable for optical rectification [41]. n_{gr}: optical group refractive indices, n_{THz} : THz refractive indices, α_{THz} : absorption coefficient, THz index, and absorption coefficient are given for 1 THz.

Material	n_{800nm}^{gr}	$n_{1.55\mu m}^{gr}$	n_{THz}	α_{THz} (cm^{-1})
CdTe		2.81	3.24	4.8
GaAs	4.18	3.56	3.59	0.5
GaSe	3.13	2.82	3.27	0.5
GaP	3.67	3.16	3.34	0.2
ZnTe	3.13	2.81	3.17	1.3
sLN	2.25	2.18	4.96	17

2.2.1. Lithium niobate

Today, lithium niobate ($LiNbO_3$, LN) is the nonlinear material in the most frequently used intense pulsed THz sources. Therefore, its properties are considered here in more detail. It has many other applications as well, being one of the most versatile optical materials. For

applications, among others, its electro-optics, piezoelectric, acousto-optic, photorefractive, pyro-electric, photovoltaic properties can be important. LN single crystals are used as an optical waveguide, piezoelectric sensors, optical modulators, and various other linear and nonlinear optical components.

LN, an artificial ferroelectric crystal, was first fabricated in Bell Laboratories in the mid-'60s. It is a colorless solid, insoluble in water. It is transparent for wavelengths between 350 and 5200 nm. It has a trigonal crystal system [44], which lacks inversion symmetry and displays ferroelectricity, Pockels effect, piezoelectric effect, and nonlinear optical polarizability of various orders, including second-order one. A conventional hexagonal unit cell of LN shown in Figure 2-2.

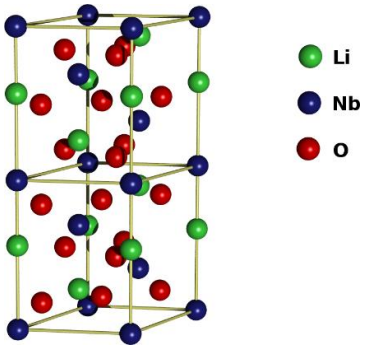

Figure 2-2 Hexagonal unit cell of LN.

The composition of LN can control its physical properties, such as the photorefraction, photo-and electrical conductivity. The optical homogeneity of crystals is directly related to structural ordering, determined mainly by the growing method. LN has negative uniaxial birefringence, which depends slightly on the stoichiometry of the crystal and temperature.

There are two basic LN crystal types: congruent LN (cLN) and stoichiometric LN (sLN). In the former case, the ratio of Li and Nb concentration is 0.945, in the latter case, it is 0.979 [45]. sLN has a lower optical damage threshold than cLN [46-48], and larger electro-optic coefficient r_{33} [49]. The precise control of stoichiometry and doping is important for controlling the physical properties of the crystal. For example, doping LN by magnesium oxide (Mg:LN) increases its resistance to optical damage (also known as photorefractive damage) [50], whereby a lower MgO concentration is needed in Mg:sLN than in Mg:cLN [48,51]. It was shown that photorefraction disappears when the Mg content exceeds a threshold value of about 0.6 mol% in sLN and 5–6 mol% in cLN [47,52-54].

The optical properties and parameters for cLN and sLN crystals can be found in references [55,56]. Palfalvi et al. reported the temperature dependence of the refractive index and absorption coefficient of sLN and cLN crystal with different MgO doping concentrations. In particular, 0.7 mol% Mg-doped sLN seems to be the most promising efficient THz source since it has a low THz absorption coefficient [57].

2.2.2. THz generation in lithium niobate

The large nonlinear coefficient of LN makes it well suitable for optical rectification. However, without further measures, the THz generation efficiency remains low because of the very different optical group and THz refractive indices. Infact, the optical group index (velocity) is smaller (larger) by more than a factor of two than the THz refractive index (phase velocity) (Table 1). Therefore, the pump pulse overtakes the THz phase fronts as they propagate through the crystal. In a velocity-matched medium, it is clear that a long crystal can be used and a large interaction length can be achieved. Hebling et al. suggested the tilting of the intensity front of the pump pulse to achieve velocity matching in LN [58]. The THz radiation that is excited by the tilted pulse front of the NIR pump propagates perpendicularly to this front with the velocity v_{THz}. The angle between the propagation direction of the THz radiation and the propagation direction of the pump pulse will be the same as the tilt angle γ of the pulse front relative to the phase front of the pump. Then, instead of Eq.(3), the magnitudes of the velocities the following equation:

$$v_{NIR}^{gr} cos\gamma = v_{THz} \tag{5}$$

If $v_{NIR}^{gr} \geq v_{THz}\left(n_{NIR}^{gr} \leq n_{Tz}\right)$, then this modified velocity matching condition can be easily fulfilled by an appropriate choice of the angle γ. Pulse front tilting of a light beam necessarily leads to angular dispersion. The connection between the pulse front tilt γ and angular dispersion for material with refractive index n is given by [59]:

$$tan\,\gamma = -\frac{n}{n_{gr}}\lambda\frac{d\varepsilon}{d\lambda} \tag{6}$$

n is the refractive index, n_{gr} is the group refractive index, λ is the wavelength and $\frac{d\varepsilon}{d\lambda}$ is the angular dispersion, where:

$$n_{gr} = n - \lambda\frac{dn}{d\lambda} \tag{7}$$

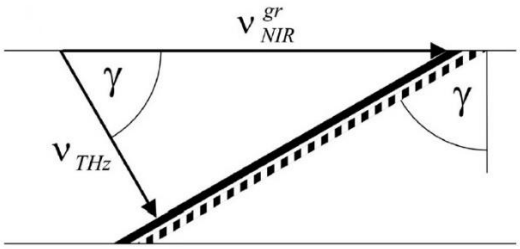

Figure 2-3. Illustration of velocity matching using tilted-pulse-front [41].

Optical rectification of ultrashort laser pulses with tilted pulse front in LN [58] has implemented as a reference technique for efficient THz generation. In THz generation experiments, perpendicular incoupling of the pump and perpendicular outcoupling of the THz beam are the conditions of minimizing reflection losses and avoiding the angular dispersion of the THz beam. Therefore a prism-shaped LN crystal is used with a large wedge angle equal to the pulse-front tilt (63°). The illustration of velocity matching using tilted-pulse-front depicted in Figure 2-3.

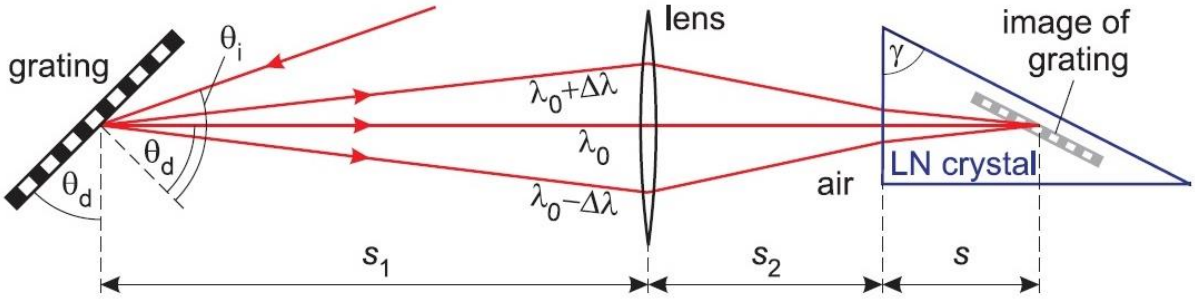

Figure 2-4. Tilted-pulse-front-pumping setup [60].

Figure 2-4 shows the pulse-front-tilting setup and its parameters, θ_i and θ_d are incidence and diffraction angle at the grating, respectively. θ_d also gives the tilt angle of the grating. The distance s between the image of the grating and the crystal input surface along the optical axis. The s is arbitrarily chosen so that the region of effective THz generation (gray-shaded area in Figure 2-4) is not truncated. The geometrical parameters of the setup (Figure 2-4)[60]:

$$sin\theta_d = \frac{\lambda_0}{n(\lambda_0)n_{gr}(\lambda_0)p}a \tag{8}$$

$$sin\theta_i = {}^{\lambda_0}/_{p} - sin\theta_d \tag{9}$$

$$S_1 = f(\sqrt{a} + 1) \tag{10}$$

$$S_2 = \frac{fS_1}{S_1 - f} - \frac{S}{n(\lambda_0)} \tag{11}$$

$$a = \frac{n^2(\lambda_0) n_{gr}(\lambda_0) p}{2\lambda_0} \sqrt{\frac{\lambda_0^2}{n_{gr}^2(\lambda_0) p^2 tan^4\gamma} + \frac{4}{n^2(\lambda_0)}} - \frac{n^2(\lambda_0)}{2tan^2\gamma} \tag{12}$$

Where λ_0 is the central wavelength, *p* is the grating period, *f* is the focal length of lens, s can be chosen according to the spot size and it is typically 1 – 5 mm. In order to obtain optimal pump-to-THz conversion and optimal THz beam characteristics, the setup has to fulfill the following criteria: velocity matching of pump pulse and THz, the pump pulse duration has to be minimal across the tilted pulse front and the pump pulse front has to be plane in the crystal [60].

Tilted pulse front allows further up-scaling of the THz energy by using a larger pump spot size and stronger pump pulse [61], another way higher efficiency could be achieved by (i) Decreasing the temperature of LN, since the absorption coefficient of LN in the THz range reduces with decreasing temperature, thus the THz efficiency will be higher at low temperatures [57]. Figure 2-5 shows that the absorption coefficient of LN depends on temperature. (ii) Using longer pump pulse, the THz spectrum is shifted to lower frequency, which reduces absorption within the crystal [62]. In addition to the longer pump pulse duration also allows a longer THz generation length [60]. It was reported that the most substantial limitation to THz generation in LN for pumping at 1 μm is frequency down-shift and the spectral broadening (cascading effect) of the optical pump pulse in conjunction with large angular dispersion of the tilted-pulse-front [63].

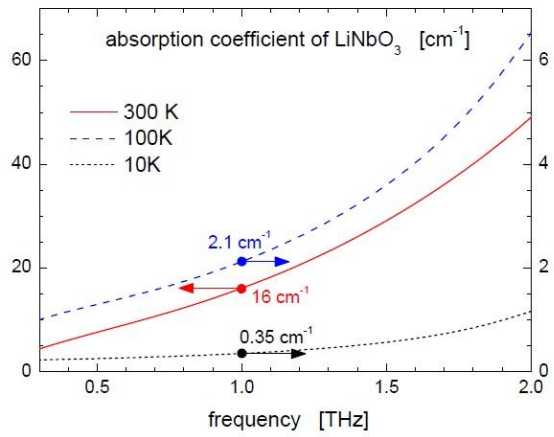

Figure 2-5. Frequency dependence of the absorption coefficient of LN in the THz range for different temperatures (left Y-axis is the absorption coefficient of LN [cm^{-1}]) [62].

Since the diffraction efficiency of a grating is usually maximal in Littrow-geometry, using an incidence angle close to the Littrow-angle $\theta_{Littrow} = sin^{-1}(\lambda_0/2p)$ will be advantageous. Challenging to get higher THz energy in tilted-pulse-front pumping by increasing the pump energy and spot size bumped into some of the limits. A prism-shaped LN crystal with a large wedge angle equal to the pulse –front tilt (63^0) results in a non-uniform pump propagation length across the beam. Such a source geometry can lead to a spatially varying interaction length for THz generation [60]. Different approaches have been proposed to mitigate the limitations of the tilted-pulse-front pumped THz source. Omitting imaging optics and bringing the grating directly in contact with the nonlinear crystal has an advantage that is reducing imaging error. The larger pumped area can be efficiently used when the imaging error is eliminated, resulting in higher THz energy and better beam quality [64,65]. The unsolved fabrication technological problem concerning the development of LN contact grating brought up the idea to create the hybrid-type THz pulse source, which combines the conventional and the contract grating setup [66]. In this setup, the pulse-front-tilt is produced in two steps, first by diffraction on the conventional grating followed by diffraction on the contact grating. Since the tilt angle is smaller than previous, imaging errors are reduced, but the necessary wedge angle (~30^0) is still large enough to make an asymmetric beam.

That is especially problematic in the case of high energy THz generation, where a wide pump beam is needed. A modified version of The tilted-pulse-font THz generation was demonstrated by reflecting the pump beam on a stair-step echelon. A segmented titled-pulse-front is formed in this setup, instead of a continuous pulse-front. Reflective echelon used for tilting the average pump pulse front for efficient THz generation in LN, but this setup still requires a prism-shaped LN crystal with the same γ wedge angle as in the conventional setup [67,68]. A modified hybrid approach to provide uniform interaction length across the large pump and THz beams was proposed [69]. In this setup, a conventional scheme containing diffraction optics and imaging is combined with a nonlinear medium. The nonlinear medium is a plane-parallel LN slab with an echelon structure on its input surface. Hence the absorption and dispersion are uniforms across the output THz beam profile. Inside the LN slab, a segmented tilted pulse front is formed with an average tilt angle as required by phase matching. The advantage of this setup is to reduce imaging error. It may lead to the realization of a scalable THz pulse source with excellent beam quality.

2.2.3. Semiconductor nonlinear materials for optical rectification

Experimental work in the early 1990s reported that THz frequency radiation could be generated by femtosecond optical pulses incident on a semiconductor [70]. The intensity of the emitted THz radiation observed when the crystal was rotated about its surface normal indicated that there was more than one mechanism responsible for the generation of THz radiation. Chuang et al. proposed a theoretical model based on optical rectification of femtosecond laser pulses at semiconductor surfaces [71], which successfully explained all of the earlier experimental observations. The investigation of the physics of optical rectification indicates that depending on the optical fluence. The THz radiation generation by optical rectification is either a second-order nonlinear optical process governed by the bulk second-order susceptibility tensor or a third-order nonlinear optical process [72,73].

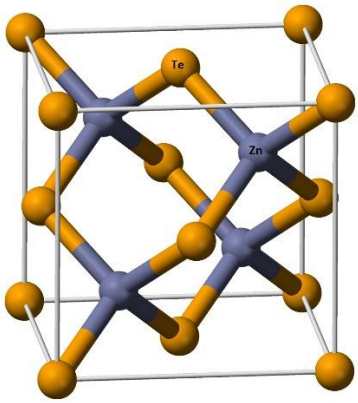

Figure 2-6. The zinc-blende type crystal structure of ZnTe.

THz radiation generation from optical rectification of femtosecond laser pulses has been reported from [100], [110], and [111] oriented crystals with zincblende structure (Figure 2-6), common for several semiconductors [36,74]. These crystals belong to the crystal class $\bar{4}3m$ and have three nonvanishing contracted matrix elements and only one independent: $r_{14} = r_{25} = r_{36}$ [20]. When an optical field interacts with these crystals, its THz radiation power depends on the direction of the field in the crystal frame. In case of the most frequently used [110] oriented crystals, the dependence of the THz output power on the angle θ (the angle between the polarization of the optical pump beam and the [0, 0, 1] *Z*-axis) can be expressed as [75,76]

$$|E_{THz}| \propto |P| = 2\varepsilon_0 d_{eff} E_0^2$$
$$= \varepsilon_0 d_{14} E_0^2 [sin^2 2\theta + sin^4 \theta]^{1/2} \quad (13)$$

Where E_0 is the amplitude of the pump field, P is the nonlinear polarization, ε_0 is the vacuum permittivity and d_{eff} is the effective nonlinear coefficient and is related to d_{14}, for zincblende structure $d_{eff} = d_{14}[sin^2 2\theta + sin^4\theta]^{1/2}/2$.

Experiments conducted on oriented [100], [110] and [111] GaAs, CdTe and InP crystals [36,72,77] and [110] GaP [38] crystal are in agreement with the theoretical results providing evidence that second-order bulk optical rectification is the major nonlinear process under the condition of certain optical fluence and normal incidence on unbiased semiconductors.

Among the zincblende crystals, ZnTe is the most popular candidate for the generation of THz radiation by optical rectification. ZnTe is a semiconductor material with a direct bandgap of 2.26 eV [78]. ZnTe has relatively large second-order nonlinear susceptibility and it has a favorable phase-matching condition with 800 nm light that allows it to produce large-amplitude, broad-bandwidth pulses in the far-infrared. Nahata et al. [43] first reported THz generation and detection using [110] ZnTe crystal, pumped by 130 fs pulse at 800 nm from Ti:sapphire laser. THz Energies up to 1.5 μJ per pulse with a spectral range extending to 3 THz and an energy conversion efficiency of 3.1x10-5 were obtained from [110] ZnTe pumped by a 100 Hz Ti:sapphire laser source [79]. However, the scaling up of THz pulse energy generated in ZnTe from 800 nm excitation laser pulse is limited by the saturation of the THz generation efficiency due to strong two-photon absorption of the pump.

Using a large area of ZnTe THz emitter is an alternative solution for suppressing the saturation effect due to two-photon absorption (2PA) of the pump beam and free-carrier absorption of the THz pulse [80], which reduce the efficiency of THz generation in ZnTe. It has been proved that the saturated THz conversion efficiency of ZnTe crystal mainly depends on free-carrier absorption, rather than on the pumping power, which is attenuated by two-photon absorption [81,82]. Interestingly, it was reported that increasing further the pump pulse fluence leads to a recovering of the quadratic dependence of the THz power with respect to the pumping fluence, which is usually observed at low intensity [83]. Moreover, dispersion of ultrashort femtosecond Ti:sapphire pulses in the thick ZnTe crystal also leads to a decrease in the optical rectification efficiency [82].

Gallium phosphide (GaP) is a compound semiconductor material with a direct (indirect) bandgap of 2.78 eV (2.24 eV) at room temperature. GaP has a refractive index between 3.1192 at 1. μm and 3.0509 at 1.6 μm [84]. GaP has a moderate electro-optic coefficient (d_{41} = 1 pm/V [85]) and its first transverse optical phonon frequency is lying as high as 11 THz, which

potentially offers a smooth frequency response in the < 10 THz range [86]. An optimum optical rectification for GaP with respect to the bandwidth and efficiency is reached by driving wavelength around 1 µm. Furthermore, the absorption coefficients of GaP are low in both the THz ($\alpha \sim 3$ cm-1 at 1 THz) and NIR range ($\alpha \sim 0.1$ cm-1 at 1.064 µm) [87]. Optical rectification of ultrashort $\sim$ 1 µm pulse in GaP a highly promising route towards the combination of high THz average power and broad bandwidth. Chang et al. reported THz generation in GaP pumped by a 210 fs, 10W Yb-fiber laser, providing 6.5 µW average power with a spectral width of 3.5 THz [38]. Furthermore, Li et al. showed THz pulse generation in GaP driven with a chirp-tunable sub-60 fs Yb-fiber amplifier and the average power of 82.6 µW was obtained at 9W pump power with negatively chirped pulses [88]. Xu et al. recently presented broadband THz generation by optical rectification of 20 fs pulses spectrally centered at 1 µm with an average power of 5.5 W and repetition frequency of 78 MHz in a GaP crystal. The spectrum with the largest bandwidth was generated up to 5 THz with Yb-based laser systems [87].

In the development of THz sources using tilted pulse front pumping, the selection of the nonlinear material is a crucial step. The effective nonlinear coefficient, wavelength, phase matching between pump and THz field and THz absorption are the essential points to consider. Table 2 list some of the nonlinear materials most suitable for optical rectification.

Table 2. List of nonlinear material are most suitable for optical rectification [60]. d_{eff} : effective nonlinear coefficient for optical rectification, λ_0 : pump wavelength, 1PA, 2PA, 3PA : linear, two-photon, three-photon absorption respectively

Material	d_{eff} [41] [pm/V]	λ_0 = 800 nm		λ_0 = 1064 nm	
		γ	Pump absorption	γ	Pump absorption
CdTe	81.8	-	1PA	9.6^0	2PA
GaAs	65.6	-	1PA	-	2PA
GaSe	28.0	16.5^0	2PA	25.9^0	2PA
GaP	24.8	-	2PA	9.3^0	Indirect 2PA
ZnTe	68.5	collinear	2PA	22.4^0	2PA
LN	168	62.7^0	3PA	63.4^0	4PA

As an example, ZnTe has direct-bandgap 2.26 eV; for pumping wavelength above 1650 nm, the 4PA and higher-order MPA are effective (Figure 2-7 (a)). Data of wavelength MPA cut-off for different few material up to 2.5 µm shown in Figure 2-7 (b).

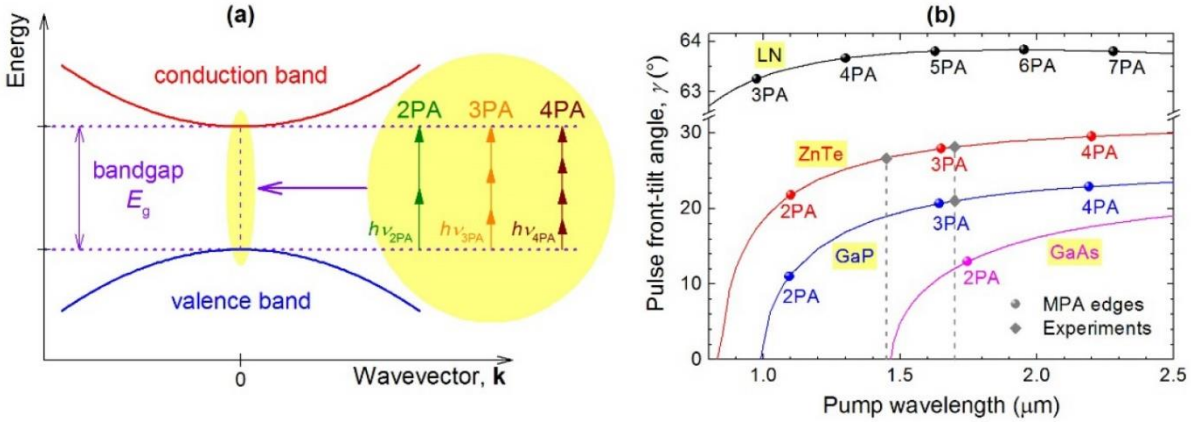

Figure 2-7 (a) schematic band structure of ZnTe. (b) PFT angle versus pump wavelength for phase matching at 1 THz in LN and selected semiconductors. [89]

At longer pump wavelengths, it is possible to reduce low-order multiphoton absorption (MPA) in semiconductors [40,60]. F. Blanchard et al. successfully produced THz pulses with 0.6 μJ energy, at $5x10^{-4}$ efficiency by pumping GaAs at a wavelength of 1.8 μm. This wavelength is sufficiently long to suppress two-photon absorption [90]. The collinear pumping can not be used because using longer pump wavelength. The pulse front tilt is necessary for velocity matching even much smaller than for LN. Semiconductors such as GaAs or GaP have lower THz absorption, together with the significantly maximal THz generation length resulting from the much smaller pulse front tilt can get higher THz efficiency than in LN [60]. Polonyi et al. reported that THz pulse with 14 μJ energy was generated with as high as 0.7 % efficiency in ZnTe pumped at 1.7 μm using tilted-pulse-pump pumping [89]. It is shown that scaling the THz pulse energy from semiconductor crystal was feasible by increasing the pump spot size and pulse energy.

2.2.4. Multicycle THz pulse generation

Intense nearly single-cycle terahertz (THz) pulses can be used in material science [91] and for the acceleration of electrons [92] and protons [93,94]. The waveguide and resonator structures proposed for electron acceleration can be even more efficiently driven by multicycle THz pulses. Dielectric grating structures were proposed for laser-driven electron acceleration [95], where using multicycle THz pulses, rather than optical pulses, can be of significant advantage. Multicycle THz pulses also could be used as drivers of coherent X-ray generation [96] and electron beam diagnostics. Multicycle narrowband THz pulses with lower peak amplitude, but higher spectral brightness may serve as a way of circumvent such electronic responses and still

maintain high exciting strength for resonant driving in particular electronic, lattice or magnetic nonlinear responses [97].

Multicycle THz pulse could be generated by tilting the intensity front of a quasi-sinusoidal intensity-modulated optical waveform on LN crystal [98] and using LN planar waveguide [99]. On the other hand, multicycle THz pulses have been generated using the structure of periodically poled lithium niobate (PPLN) crystal [100-102]. Since organic crystal, HMQ-TMS has been shown to generate intense broadband THz pulse [103], the generation of continuously tunable multicycle THz pulse using this crystal had been reported and produced the center frequency from 0.3 to 0.8 THz [97]. The superposition of signal and idler pulses in dual-chirped optical parametric amplification was proposed for efficient generation of intensity-modulated pulses with periodic modulation. The numerical simulation for a three-stage optical parametric amplifier system predicted an efficiency as high as 50% for about 40 mJ of output pulses energy, which could be suited for driving intense multicycle THz pulse generation sources [104].

It was recently demonstrated that nonlinear semiconductor materials offer a promising alternative with scalability to highest THz pulse energies and field strengths [40,105-108], also enabling the construction of monolithic contact-grating sources [106]. Lee et al. showed the generation of multicycle narrow-bandwidth THz pulses in periodically inverted GaAs structures using optical rectification at 2 μm wavelength [109]. In order to avoid the associated free carrier absorption in the THz range, semiconductor materials need to be pumped at a sufficiently long infrared wavelength to suppress two- and three-photon absorption [106,107].

2.3. THz pulse characterization

2.3.1. Power/Energy measurement

Thermal detectors are usually used for detecting THz radiation. The fundamental element of thermal sensors is a radiation THz absorber attached to a heat sink. Radiation energy absorbed by thermal absorber is converted into heat and a thermometer part measures the temperature changes induced by THz. The absorbed THz radiation energy is determined by calibrating the output measurement.

Pyroelectric crystals are spontaneously polarized crystals, and each unit cell has a permanent electric dipole moment, aligned with a specific crystal axis [20]. The level of this spontaneous electric polarization depends on the temperature. The spontaneous polarization is accompanied by surface charge, neutralized by free carriers forming a steady state.

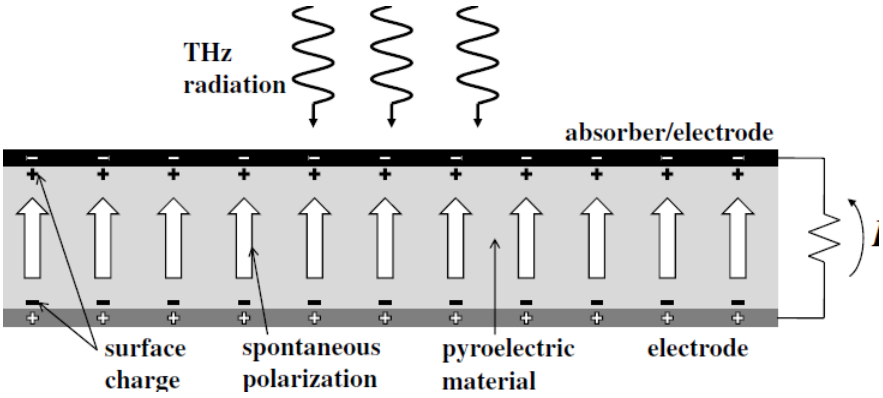

Figure 2-8. Schematic diagram of a typical pyroelectric detector [20].

Figure 2-8 shows the basic scheme of a pyroelectric detector. The pyroelectric crystal cut perpendicular to its polar axis is sandwiched between two electrodes. One side is usually treated to absorb incident radiation. The radiation generated heat raises the temperature of the pyroelectric crystal and induces a reduction of the spontaneous polarization and the surface charge [20]. The attached electrodes on the two opposite crystal surfaces form a capacitor. If the circuit is closed, a current flows through it to compensate for the change in the surface charge. Large load resistance is applied to achieve high responsivity and the signal is improved further by an operational amplifier. These detectors are used with light pulses because no pyroelectric current is generated in a steady-state.

2.3.2. Electro-optic sampling

In the ultrafast electronics and optoelectronics communities, especially in the subfield of applied terahertz beams, the detection of freely propagating picosecond microwave and millimeter-wave signals is primarily being carried out via photoconductive antennas and far-infrared interferometric techniques [110,111]. The detection of electro-optic sampling for the characterization of ultrafast electrical transients had been reported by Valdamis [112].

Electro-optic detection of THz radiation is based on the measurement of the phase modulation induced on the light pulse by the THz pulse as both pulses propagate through the electro-optic crystal. Free-space electro-optic sampling measures the actual electric field of THz pulses in the time domain, determining not only the amplitude but also the phase. The mechanism of electro-optic sampling is based on the Pockels effect, whereby through proper velocity matching the measured waveform can be cross-correlation of the incident terahertz and optical pulses [113]. Fundamentally, the electro-optic effect is a nonlinear coupling between an electric field (THz pulse) and a laser beam (optical pulse) in the sensor crystal.

The Pockels effect is closely related to optical rectification, which is apparent in the similarity of second-order polarization.

$$P_i^{(2)} = 2\sum_{j,k} \epsilon_0 \chi_{ijk}^{(2)}(\omega, \omega, 0)\, E_j(\omega) E_k(0)$$

$$= \sum_{j} \epsilon_0 \chi_{ij}^{(2)}(\omega)\, E_j(\omega) \qquad (14)$$

where $\chi_{ij}^{(2)}(\omega) = 2\sum_k \chi_{ijk}^{(2)}(\omega, \omega, 0)\, E_k(0)$ is the field-induced susceptibility tensor. The Pockels effect has the same nonlinear optical coefficients as optical rectification. Eq.(14) indicates that a static electric field induces birefringence in a nonlinear optical medium proportional to the applied field amplitude. Then the applied field strength can be determined by measuring the field-induced birefringence.

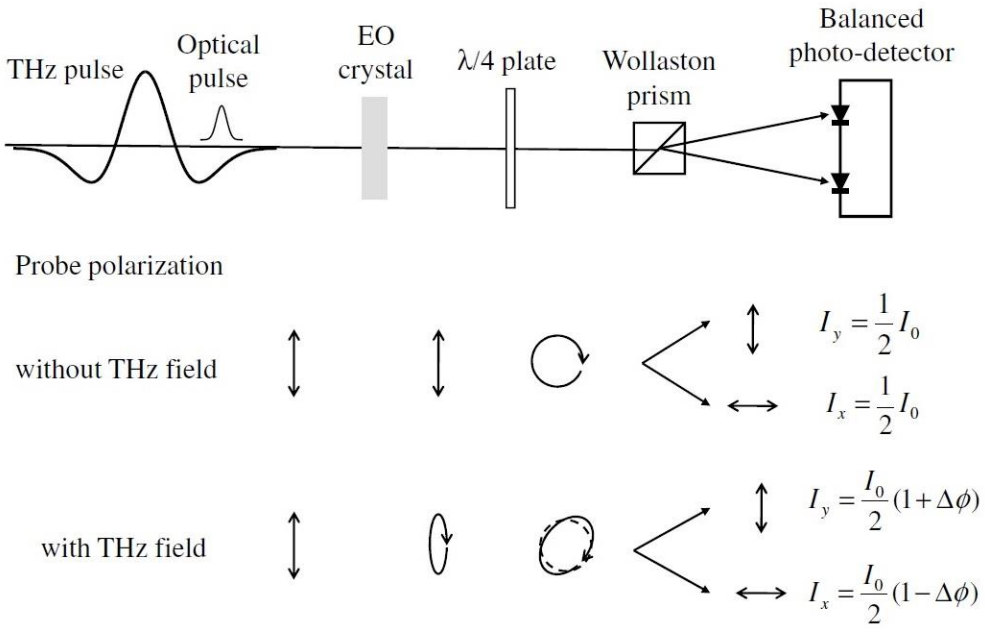

Figure 2-9. Schematic diagram of a typical setup for electro-optic sampling [20].

The coherent detection of free-space THz pulses can also be realized with a high signal-to-noise ratio in the electro-optic nonlinear crystal once the phase-matching condition is satisfied. Figure 2-9 illustrates a typical setup of free-space electro-optic sampling to measure field-induced birefringence. Ideally, the optical group velocity matches the THz phase velocity in the electro-optic crystal. The optical pulse will detect a constant electric field of the THz pulse while propagating. In the lower part of Figure 2-9, the evolution of the probe polarization is shown in series for the steps of the polarization manipulation with or without a THz field. While the linearly polarized optical pulse and the THz pulse propagate through the electro-

optic crystal, modulating the birefringence of the sensor crystal via an applied. The polarized electric field will modulate the polarization ellipticity of the optical probe beam passing through the crystal. The ellipticity modulation of the optical beam can then be polarization analyzed to provide information on both the amplitude and phase of the applied electric field [113]. When pulsed electromagnetic radiation (THz beam) illuminates the electro-optic crystal, the index of refraction is modulated via the Pockels effect. A femtosecond optical pulse probes the field-induced change in the index of refraction by passing the optical beam through the crystal. A Wollaston prism splits the probe beam into two orthogonal components, which are sent to a balanced photo-detector. The detector measures the intensity difference $I_s = I_y - I_x$ between the two orthogonal components of the probe pulse, which is proportional to the applied THz field amplitude [20]. By varing the delay between the THz beam and the optical probe beam, one obtains the complete time-dependent electric field.

For electro-optic sampling, zinc-blende crystals such as ZnTe and GaP are often used. The useful characteristics of ZnTe crystal for THz generation (like high transparency at optical and THz frequencies, large electro-optic coefficient) are also desirable for efficient electo-optics sampling. ZnTe is also suitable because its refreactive index in the far-infrared is comparable to the near-infrared refractive index, resulting in relatively efficient THz detection [114].

The differential phase retardation $\Delta\phi$ experienced by the probe due to the Pockels effect over a propagation distance L is given as [37]

$$\Delta\phi = \left(n_y - n_x\right)\frac{\omega L}{c} = \frac{\omega L}{c} n_o^3 r_{41} E_{THz} \tag{15}$$

where n_o is the refractive index at the optical frequency and r_{41} is the electro-optic coefficient. The intensity of the two optical probe beams at the balanced photodetector are

$$I_x = \frac{I_o}{2}(1 - \sin\Delta\phi) \approx \frac{I_o}{2}(1 - \Delta\phi)$$

$$I_y = \frac{I_o}{2}(1 + \sin\Delta\phi) \approx \frac{I_o}{2}(1 + \Delta\phi) \tag{16}$$

where I_o is the incident optical probe intensity, and we asume $\Delta\phi \ll 1$ for the approximation. Thus, the signal of the balanced photo-detector measures the THz field amplitude

$$I_o = I_y - I_x = I_o\Delta\phi = \frac{I_o \omega L}{c} n_o^3 r_{41} E_{THz} \propto E_{THz} \tag{17}$$

In the experiment, the temporal or spectral resolution of electro-optic sampling is limited by three factors: (i) finite pulse duration of optical probe, (ii) dispersion of nonlinear susceptibility, and (iii) mismatch between optical group and THz phase velocity [20].

For the ZnTe, the efficiency of THz detection strongly depends on the orientation of the THz polarization with respect to the crystal [001] axis and on the angle between the optical probe polarization and the THz polarization. The optimum angles between the THz and the optical probe beam polarization are 0^0 and 90^0 [114]. Among the various electro-optic materials, ZnTe shows the highest field sensitivity near 2 THz [115]. However, because the first transverse optical phonon resonance of ZnTe lies at 5.3 THz, the dispersion and absorption associated with this resonance limit the high-frequency response of the ZnTe sensor to 5 THz. GaP is an indirect zincblende semiconductor having its first transverse optical phonon resonance near 11 THz. It was reported that GaP could be used as an electro-optic sensor to detect up to 7 THz [116].

2.4. Multiphoton Absorption

2.4.1. Measurement of nonlinear absorption

Numerous techniques are known for the measurement of the nonlinearity of optical materials. Nonlinear interferometry, degenerate four-wave mixing, nearly degenerate three-wave mixing, ellipse rotation, and beam-distortion measurement are the techniques frequently reported. Interferometry and wave mixing are potentially sensitive techniques but require a sophisticated experimental instrument, while beam-distortion measurements require precise beam scans [117]. The Z-scan measurement is one of the most frequent techniques used for measuring the strength of the Kerr nonlinearity (i.e., the magnitude of the nonlinear index n_2) and the nonlinear absorption of an optical material.

Based on the principles of spatial beam distortions, Sheik-Bahae et al. proposed a single beam experimental technique, known as Z-scan [117] in 1989, for characterization of nonlinear optical materials. The name Z-scan stems from the fact that in this technique, the sample is scanned along the direction of propagation of the incident laser beam, which is conventionally taken as the Z-axis. A lens focuses the incident Gaussian laser beam and the sample is scanned along the waist of the beam using a motorized translation stage (Figure 2-10). The transmittance of the nonlinear medium is measured as a function of the sample position (Z) through a finite aperture placed in the far-field. As the sample is translated along the focused Gaussian beam, it experiences different incident field strength at different Z-positions. The

accuracy of determination of the nonlinear coefficients γ (nonlinear refraction) or β (nonlinear absorption) depends on competing nonlinearities, a model of the nonlinearity of material and how precisely the laser source is characterized in terms of its temporal and spatial profiles, power or energy content and stability [118].

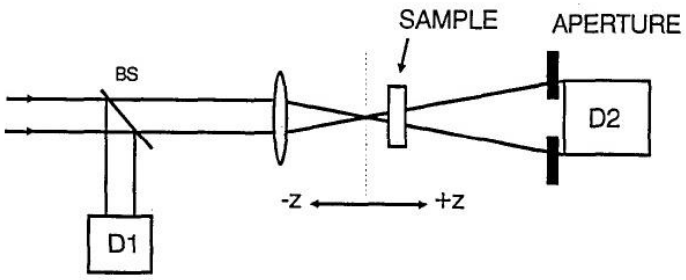

Figure 2-10. Z-scan setup scheme [117]. D1 and D2 are detectors, and BS is beam splitter.

The nonlinear refraction in the sample arising from the nonlinearity manifests itself as intensity-dependent convergence or divergence of the transmitted beam (self-focusing/defocusing). Therefore, the light passing through an aperture placed in a far-field will vary with the sample position. Consequently, the aperture transmittance is a function of the sample position Z. The sign of the nonlinear refraction is readily obtained from a Z-scan signal. An increase in transmittance in the pre-focal region followed by a decrease in the post-focal region (peak-valley) in the Z-scan signal denotes negative nonlinear refraction, whereas a valley-peak configuration denotes a positive nonlinearity [119].

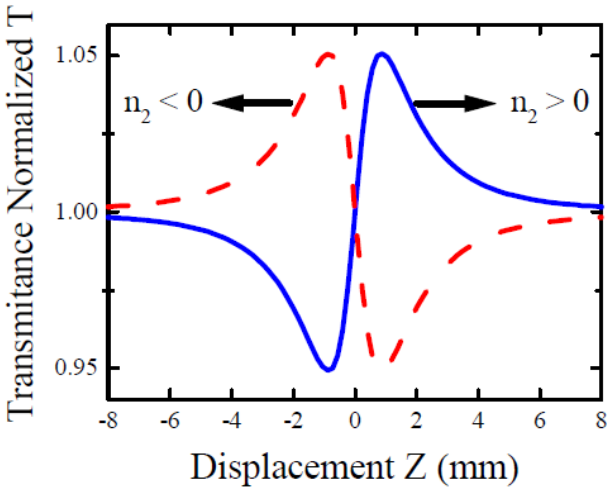

Figure 2-11. A typical Z-scan for positive (blue solid line) and negative (red dashed line) nonlinear refraction [120].

In a thin nonlinear sample with cubic nonlinearity, the sample at position z has a linear refractive index n_o and a more general refractive index n, which depends on the irradiance $I(x, y, z)$. For a Kerr nonlinearity [119],

$$n = n_o + \gamma I = n_o + \frac{1}{2} n_2 |E|^2, \tag{18}$$

where n_2 is the linear index of refraction, E is the electric field amplitude within the sample (cgs), and I is the irradiance (MKS). The coefficient γ and n_2 are related through the conversion formula [119]

$$n_2(esu) = \frac{c n_o}{40\pi} \gamma (m^2 W^{-1}), \tag{19}$$

where $c\ (ms^{-1})$ is the speed of light in a vacuum. In a thin nonlinear sample, there is insufficient path length for the beam to change its size or shape as it propagates through the medium. The effect of the nonlinearity is a phase change $\Delta\phi_o$ at the nonlinear medium.

$$\Delta\phi(r, z) = k\gamma I(r, z) L_{eff}, \tag{20}$$

where $k = 2\pi/\lambda$, λ is wavelength, and L_{eff} is the effective sample length. $L_{eff} = (1 - e^{-\alpha_o L})/\alpha_o$, where L is the true sample length and α_o is the linear absorption coefficient. Here, the irradiance of a Gaussian beam, with waist size w_0 and waist at z = 0 is

$$I(r, z) = \frac{I_0 e^{-2r^2/w(z)^2}}{1 + z^2/{z_R}^2}, \tag{21}$$

where

$$w(z)^2 = {w_0}^2 (1 + \frac{z^2}{{z_R}^2}), \tag{22}$$

and the Rayleigh length is $z_R = \pi {w_0}^2/\lambda$. The nonlinear phase shift is

$$\Delta\phi_0 \equiv k\gamma I(0, z) L_{eff} = \frac{\Delta\Phi_0}{1 + z^2/{z_R}^2}, \tag{23}$$

where $\Delta\Phi_0 \equiv k\gamma I_0 L_{eff}$, I_0 is the axial irradiance at the waist.

The nonlinearity can be evaluated from the difference between the maximum (peak) and minimum (valley) values of the normalized transmittance, $\Delta T = T_p - T_v$. The normalized transmittance measured using an infinitesimal aperture at the observation plane is given to first order in irradiance by [121]

$$\mathrm{T} = 1 - \frac{4\Delta\phi_0 v}{9 + v^2} \tag{24}$$

where υ is the linear phase $\upsilon = -\frac{1}{Z_R}(z + \frac{{Z_R}^2+Z^2}{Z_1-Z})$, if z_1 is much larger than z and z_R, then $\upsilon \approx -z/z_R$. For thin optical Kerr medium with nonlinear refractive index coefficient γ, ΔT is proportional to the nonlinear phase shift $\Delta\Phi_o$ on the axis with the sample at the waist [119], and hence to γ:

$$\Delta \mathrm{T} = 0.406|\Delta\Phi_o| \tag{25}$$

Eq. (25) is correct in the first order of I_0 (the weak interaction regime), for a Gaussian profile laser beam and an infinitesimal aperture of pinhole at the far-field [122].

Removal of the aperture, i.e., collecting all the light on the detector, which is referred to as an open aperture Z-scan, will result in a flat response for a purely refractive nonlinearity. It is because the sensitivity to nonlinear refraction is entirely due to the aperture, and its removal eliminates the effect. Nonlinear absorption effect such as 2PA can be incorporated using an irradiance-dependent absorption coefficient α,

$$\alpha = \alpha_0 + \beta I = \alpha_0 + \alpha_2|E|^2, \tag{26}$$

where α_0 is linear absorption. The nonlinear absorption coefficient β and α_2 are related by

$$\alpha_2(esu) = \frac{n_o c}{8000\pi}\beta(mW^{-1}), \tag{27}$$

The effect of the nonlinear absorption is to reduce the irradiance at the exit face of the sample to an amount $I_e(r,z)$.

$$I_e(r,z) = \frac{I(r,z)e^{-\alpha_0 L}}{1+\beta I(r,z)L_{eff}}, \tag{28}$$

The nonlinear phase shift associated with γ is reduced by the nonlinear absorption of the beam,

$$\Delta\phi_0(t,z) \equiv \frac{k\gamma}{\beta}\ln(1+\beta I(r,z)L_{eff}). \tag{29}$$

The nonlinear transmittance can be determined for simultaneous nonlinear refraction and nonlinear absorption, monitored using an infinitesimal aperture. In the open aperture scheme, the transmittance corrected to all orders of irradiance is [119]

$$\mathrm{T} = \frac{1}{q_o}\ln(1+q_o), \tag{30}$$

where q_0 is the on-axis absorption parameter $q_0 \equiv \beta I(0,z)L_{eff} = \frac{Q_0}{1+z^2/{z_R}^2}$ and $Q_0 \equiv \beta I_0 L_{eff}$. The coefficient of nonlinear absorption β can be evaluated using

$$\Delta T = \left|1 - \frac{1}{Q_o}\ln(1 + Q_o)\right|, \tag{31}$$

However, if nonlinear absorption is also present, then it will be reflected as a transmission variation in the open aperture scan. Multiphoton absorption suppresses the peak and enhances the valley (Figure 2-12), while saturation of absorption produces the opposite effect in the closed-aperture Z-scan.

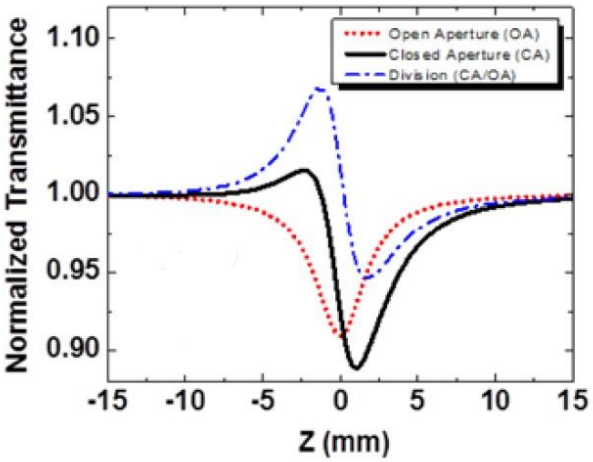

Figure 2-12. Open aperture (red dot line) and closed aperture (solid black line) Z-scan [123]

There are several factors which may lead to poor Z-scan profiles and unrealiable data: (i) a weak input beam spatial profile, (ii) poor understanding of the temporal characteristics of the laser, (iii) fluctuating laser power, (iv) sample thickness (v) inappropriate size or distance, or poor alignment of the aperture for measuring on-axis transmittance, (vii) wedge and lens effects and other defects in the sample, and (viii) laser power exceeding the range of the low power regime [122].

2.4.2. Measurement of multiphoton absorption in semiconductors

Semiconductor materials have been playing important roles in many photonics-based technologies for decades. Novel high-power ultrashort-pulse laser and parametric sources, operating at infrared wavelengths, have recently enabled new application areas in nonlinear optics [124,125]. For example, extremely efficient terahertz pulse generation has been demonstrated by optical rectification of infrared pump pulses in semiconductors [60,105-108,126]. THz-pulse-driven high-harmonic generation recently demonstrated in GaSe semiconductor [127], may enable to explore and exploit electron wavefunctions and the band structure by all-optical methods and even lead to the construction of intense CEP-stable solid-state attosecond sources. To design and optimize setups and devices utilizing intense optical

driving of semiconductors, the knowledge of their nonlinear optical parameters, such as the nonlinear refractive index or multiphoton absorption coefficients, is very important.

Theoretical scaling laws for multiphoton absorption coefficients were given for direct-bandgap semiconductors based on a two-band model [128]. An early summary of theoretical models and experimental values of two- (2PA) and three-photon absorption (3PA) coefficients for a few selected materials can be found in Ref. [129]. 2PA and 3PA of semiconductors were extensively studied experimentally in the past. The anisotropy of 2PA in GaAs [130,131] and CdTe [130] was studied with nanosecond and 30-ps pulses and found to reflect the anisotropy of the band structure because of large 2PA-generated free carrier absorption. The most commonly used method to measure 2PA and 3PA coefficients is the Z-scan technique [119].

Z-scan calculates multiphoton absorption coefficients following the assumption that only one type of multiphoton absorption dominates for a given wavelength. Then, the optical intensity, $I(z,r,t)$ can be described by

$$\frac{dI(z,r,t)}{dz} = -\alpha_N I(z,r,t)^N, \tag{32}$$

where z is propagation distance, r transverse coordinate, t time, and α_N an N-photon absorption coefficient [132]. By integrating Eq. (32) over z, r, and t, the transmitted pulse energy as a function of the peak incoming intensity I_{in} can be found, and thus normalized transmission T/T_0, where T_0 is the transmission in the low-intensity limit. When $(T-T_0)/T_0 \ll 1$, it is straightforward to show by simple integration of Eq. (32) that, in the case of Gaussian laser pulses (in space and time),

$$\frac{T_0}{T} = 1 + \frac{1}{N^{3/2}}\alpha_N I_{in}^{N-1} l, \tag{33}$$

where l is the sample thickness. Hence, near the origin, (T/T_0) versus I_{in} is a linear function (2PA), parabola (3PA), cubic parabola (4PA), etc [132]. The multiphoton absorption process of different orders can be distinguished by changing the laser wavelength. Multiphoton absorption coefficients were deduced by best fitting the numerical solution of Eq. (32) to the experimental data for open-aperture Z-scan in the whole range of transmission change, not only $(T-T_0)/T_0 \ll 1$.

Z-scan was applied to measure the tensor properties (anisotropy) [133], by using the three nonlinear eigenpolarizations [134], and the dispersion of third-order nonlinearities (2PA) [133,135] in various semiconductors. The dispersion and the anisotropy of 2PA and 3PA in

GaAs were measured in the 1.3–2.5 μm wavelength range by 100-fs pulses [132]. 3PA spectra were calculated using a four-band model and compared to measurements in direct-band-gap semiconductors [136,137]. A maximum in the 3PA coefficient was found both in theory and experiment near the 3PA cut-off wavelength.

In contrast, little is known about the four-photon absorption (4PA) and nonlinearities of even higher-order in semiconductors and other important optical materials. Recently, multi-photon absorption in GeSbS chalcogenide glass up to the 11th order was reported for wavelengths between 1.1 μm and 5.5 μm [138], and values on the order of 10^{-4} cm^5/GW^3 was found for the 4PA coefficient. This knowledge can be crucial for applications driven by infrared pulses. For example, in the newly developed very perspective semiconductor THz generators, 4PA can be a significant design issue [108,139]. The efficiency of THz generation in ZnTe could be increased by two orders of magnitude, from 3.1×10^{-5} [79] to as high as 0.7% [106,107]. The reason for this enormous increase was the elimination of both 2PA and 3PA by a sufficiently long pump wavelength [40,60,105-107,126,140], thereby eliminating the associated free-carrier absorption in the THz range. However, 4PA can still be a limiting factor for THz generation in this case. A first attempt to estimate the 4PA coefficient in ZnTe was made based on THz generation results [108], but this approach is very indirect and therefore subject to uncertainties. GaP is another semiconductor nonlinear material of high interest for efficient THz generation [108,139], but no experimental data on its 4PA coefficient are available. Thus, there is a clearly perceived lack of knowledge on important material data.

3. SCIENTIFIC GOAL

The utilization of THz radiation currently has been significantly increased, supported by the development of laser and THz science and technology. The increased energy, specific properties, and characters from the available THz sources have been given an opportunity for implementation THz on widespread applications. On the other hand, to support all of it, developing of new THz sources is continuously needed. This research aimed to design and experimentally test novel THz sources.

LN THz sources based on the tilted-pulse-front technique are today the most widely used sources of intense THz pulses. Whereas they could be greatly improved by optimizing imaging conditions, pump pulse duration, and cryogenic cooling of the crystal, a major limitation remained unsolved: The strongly nonuniform interaction length in the prism-shaped nonlinear crystal leads to strongly varying THz waveform across the beam and, consequently, to reduced field strength in focus. Thus, the scaling to extremely high pulse energy and the field strength is not possible in conventional setups. Recently, concepts based on plane-parallel or slightly wedged LN slabs have been proposed to reduce or eliminate this limitation [69,141,142].

- One goal in this work was the first demonstration and characterization of THz pulse generation from such a new plane-parallel LN slab crystal with an echelon structure on the input surface.

Triggered by the fact that major limitations in LN THz sources using the tilted-pulse-front technique are caused or enhanced by the very large pulse-front tilt angle, efforts were made in recent years to adapt this technology to other materials requiring no or smaller pulse-front tilt [60]. Semiconductor materials were considered as promising candidates. Here, the major limitation was the strong two- and three-photon absorption at conventional pump wavelengths of 800 nm or around 1030 nm, and the associated free-carrier absorption at THz frequencies. The application of infrared pump wavelengths, sufficiently long to enable only four-photon and higher-order multiphoton absorption to be effective, in combination with the tilted-pulse-front technique enabled to circumvent this limitation and lead to the demonstration of highly efficient single-cycle semiconductor THz sources [89,90].

- Another goal in this work was to extend the application potential of such intense and efficient semiconductor THz sources by considering their prospects for multicycle THz pulse generation. The aim was to investigate multicycle THz pulse generation by optical

rectification in the semiconductor nonlinear material GaP by numerical simulations to estimate the expected performance and to give guidelines for design optimization.

The design and optimization of infrared-pumped (single- and multicycle) semiconductor THz sources requires the knowledge of the four-photon absorption coefficient. The reason is that four-photon absorption can become a major limiting factor for the useful pump intensity in the absence of lower-order multiphoton absorption. However, according to our knowledge, no experimental data were available in the scientific literature about four-photon absorption coefficients in semiconductor materials important for THz generation.

- The third goal in this work was to measure four-photon absorption coefficients in GaP and ZnTe semiconductors.

4. RESULTS

4.1. THz generation based on echelon LN plane-parallel slab

4.1.1. Experiment

The investigated hybrid-type setup is a combination of the conventional scheme, containing a diffraction grating and imaging optics, and a nonlinear material with an echelon profile on its entrance surface (nonlinear echelon slab (NLES) Figure 4-1). Pump pulses of 200 fs pulse duration and 1030 nm central wavelength were delivered by a cryogenically cooled Yb:CaF_2 regenerative amplifier operating at 1 kHz repetition rate. Up to about 2.5 mJ pump pulse energy was used in the experiment. For phase matching in LN, a pulse front tilt about 63^0 requires at the pump wavelength of 1030 nm at room temperature. When the pump beam passes through the entrance of NLES, its pulse-front will be segmented. The envelope of the NLES entrance has to be parallel to the envelope of the segmented pump-pulse-front inside NLES, therefore $\gamma_{air} = \text{atan}\left(\frac{h}{w}\right)$, where h is the height and w is the width of one echelon step. The front-tilt angle in air (γ_{air}) about 63^0 is smaller than the conventional setup, where an angle of 77° is needed [59,143]. The smaller tilt angle is advantageous for reducing imaging errors of the grating-lens system [60].

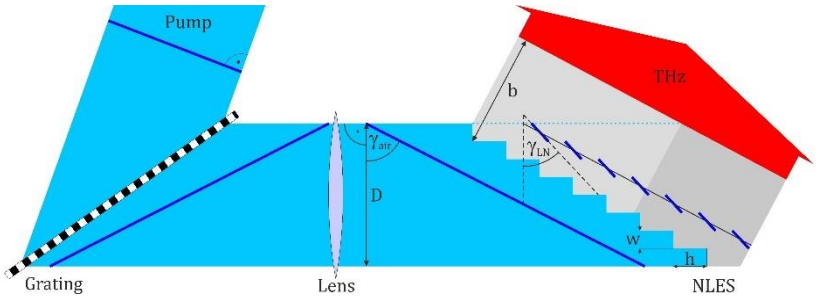

Figure 4-1. Scheme of the experimental setup. The pump pulse fronts are indicated at different positions in the setup. Angular dispersion of the pump is not shown. Inside the NLES, the pump pulse front is segmented.

The condition for the average tilt to remain unchanged while passing through the air/NLES interface is that $\gamma_{air} = \gamma_{LN}$ should hold [69]. The pulse-front-tilt in the air before entrance NLES equals the average pulse-front-tilt inside the NLES does mean that the echelon-type entrance does not influence the pulse-front-tilt. The tangent of the tilt angle would be reduced by the ratio of the group refractive indexes when the pump passes through the air/NLES interface. When the pump beam with the pulse-front tilt angle of $\gamma_{\text{air}} = 63°$ in air enters the NLES, the tilt angle reduces to $\gamma_{\text{LN}} = 42°$ (Figure 4-1), according to $\tan(\gamma_{\text{LN}}) =$

$\tan(\gamma_{\text{air}})/n_{\text{gr}}$. Here, $n_{\text{gr}} = 2.215$ is the group index of LN at the 1030 nm pump wavelength. This conditions leads to the formation of a segmented pulse front [69].

A transmission grating with 1600 mm^{-1} line density (LightSmyth Technologies, T-1600-1030S) was used at an incidence angle of 55.5°, close to the Littrow angle. To ensure the necessary pulse-front tilt at the crystal, the imaging lens (a near-infrared achromat with 25 cm focal length) had to provide a magnification of about 1.4 times. The more optimal design would involve demagnification, rather than magnification, as then the pump intensity would be higher at the crystal than at the grating. However, we had no appropriate grating to build such a setup. Grating damage was indeed limiting the useful pump intensity in our case. The pump spot size at the NLES, perpendicularly to the pump propagation direction, was 5.5 mm × 5.1 mm (horizontal × vertical, at $1/e^2$ of the peak intensity).

A prototype LN NLES device was manufactured by diamond milling (Kugler GmbH., Salem, Germany). The dimensions of the slab were 5 mm × 8 mm along and perpendicularly to the steps, respectively. The slab thickness was $L = 3$ mm. The width of the echelon steps, through which the pump beam entered the slab, was w = 50 μm (Figure 4-1). The height of the steps along the pump propagation direction was h = 92 μm. Such a step geometry is consistent with a pulse-front tilt angle of about 62°, required for velocity matching at cryogenic temperature (100 K), rather than at room temperature. For the sake of simplicity, in this proof-of-principle experiment, the NLES was used at room temperature.

The optic axis (Z-axis) of the LN slab was parallel to the (vertical) echelon lines. The slab was Y-cut. The polarization of the pump beam was perpendicular to the plane of Figure 4-1. The generated THz beam had the same polarization direction. The THz pulse energy has been measured by a calibrated pyroelectric detector (THZ 20, Sensor-und Lasertechnik). THz waveforms have been measured by electro-optic sampling in a [110]-cut 1-mm thick GaP using conventional ellipsometric balanced detection. A small fraction of the 200-fs pump pulses were used for the sampling.

Perspectival-view optical microscope images of the echelon structure are shown in Figure 4-2. The surface flatness along the entrance step faces of width w were estimated from interferometric measurements to be about $\lambda/10$ peak-to-peak at the pump wave length used here, and the rms roughness was 25 nm. It could also be deduced from microscope inspection that the step edges of the echelon profile were rounded (Figure 4-2 (b)). This resulted in an estimated reduction of the effective area by about 20% to 30%.

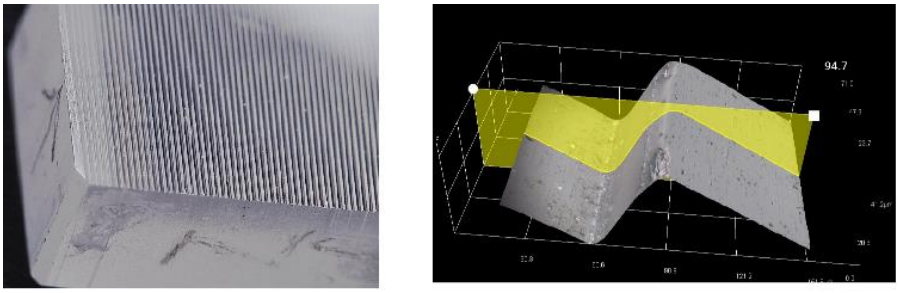

Figure 4-2. (a) Perspective view of the prototype echelon slab structure taken at 20× magnification. (b) Reconstructed surface topology model of a single step of the echelon structure (700× magnification). The images were recorded by a Hirox RH-2000 digital microscope by Emilien Leonhardt from Hirox Europe.

4.1.2. Results

Figure 4-3 shows the measured THz pulse energy (left axis) and the pump-to-THz energy conversion efficiency (right axis) as functions of the pump pulse energy (bottom axis) and the pump intensity (top axis). THz pulses with up to 1.0 μJ energy have been generated with 1.9 mJ of pump reaching the input side of the NLES. The efficiency was 5.1×10^{-4}. A nearly quadratic increase of the THz energy and a corresponding linear increase of the efficiency can be observed up to about 1.0 mJ pump energy (25 GW/cm^2 intensity). At higher pump energy (intensity), the saturation of the efficiency is observed. The useful pump energy (intensity), and consequently the THz energy, has been limited by the damage of the pulse-front-tilting grating, as mentioned above.

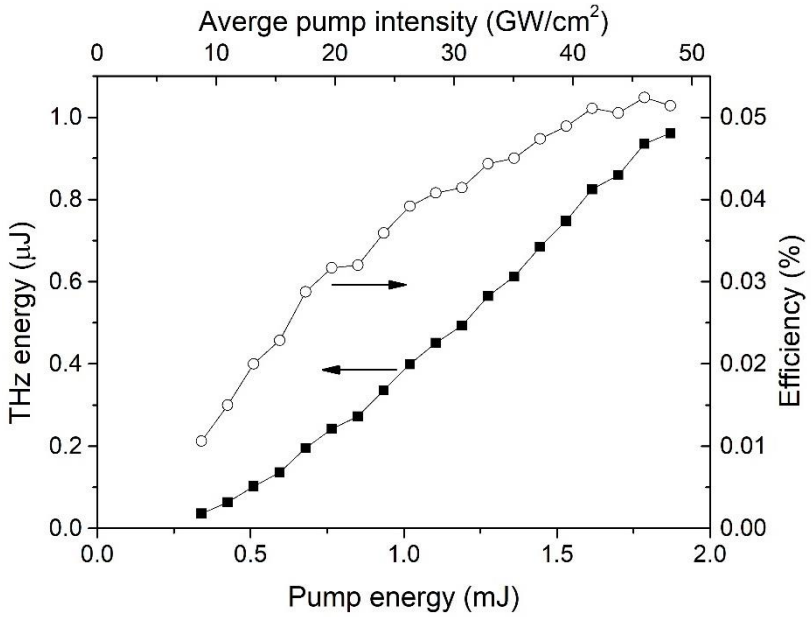

Figure 4-3 Measured THz pulse energy and THz generation efficiency as functions of the pump energy and intensity.

For comparison, the obtained THz generation efficiency was by a factor of three smaller for the NLES setup than for a conventional tilted-pulse-front pumped setup consisting of a reflection grating and an achromat lens, used for producing 77° tilt angle of the pump intensity front before the prism-shaped LN crystal with a wedge angle of 63°. According to a simple estimation, however, from this factor of three, the small size of the NLES is responsible for a factor of nearly two. For a small value of $x = D/b$ (Figure 4-4), the effective generation length will be shorter than the crystal thickness on a large part of the crystal, indicated by the light grey area inside the NLES in Figure 4-1. This causes a relative decrease in the THz generation efficiency by a factor $\eta_{\mathrm{rel}} = x^2/(3\sin^2\gamma)$ for $x < \sin\gamma$ and $\eta_{\mathrm{rel}} = 1 - 2\sin\gamma/(3x)$ for $x \geq \sin\gamma$ (Figure 4-4). In this proof-of-principle experiment, from the 8 mm full width of the NLES crystal only along a 2.4 mm broad part was the THz generation length equal to the 3 mm crystal thickness ($x \approx 1.2$), leading to a relative efficiency of $\eta_{\mathrm{rel}} = 52\%$ (indicated by the symbol in Figure 4-4) in comparison to the ideal case of $x \gg 1$. This problem can be eliminated by using crystals and pump beams with much larger transversal sizes than the thickness of the NLES. In addition, the rounded part of the echelon steps at the edges (Figure 4-2 (b)) could also have caused some efficiency decrease of the NLES setup, as compared to the ideal case.

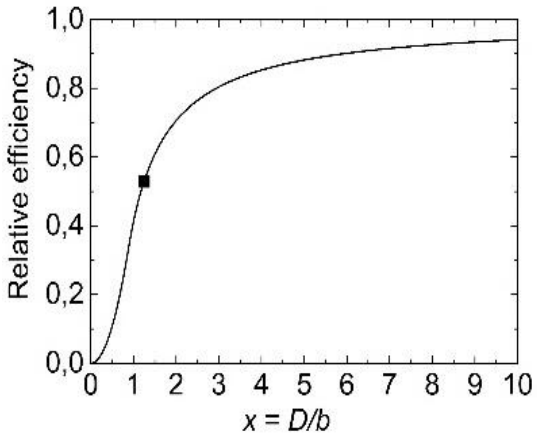

Figure 4-4 Relative THz generation efficiency owing to a reduced interaction length in the light grey area in Figure 4-1 as a function of the relative pump beam size.

By using a larger NLES of better quality, the efficiency can be expectedly improved in several ways. (i) Cryogenic cooling of the NLES reduces the absorption in the THz range and can result in a 2.5× to 3.0× increase of the efficiency [144,145]. (ii) As mentioned above, using a significantly larger NLES can result in a 2× increase of the efficiency. (iii) A larger crystal length L (5 mm instead of 3 mm) and a sufficiently large aperture can lead to still further enhancement of the efficiency by a factor of 1.3×. (iv) Because of the smaller diffraction of the segmented pump beam for a shorter wavelength of 800 nm, using a Ti:sapphire laser instead

of a Yb-based one can result in a further 40% increase of the efficiency. Taken together, improvements (i) to (iv) can increase the efficiency by about one order of magnitude, reaching $\eta = 0.5$ %.

Examples of THz waveforms measured at different pump energies are shown in Figure 4-5. These measurements have been carried out with a slightly modified setup, where a 250-cm focal length cylindrical lens has been used for imaging, in combination with a 2-m focal length cylindrical lens. This was used for the reduction of the vertical beam size at the NLES for enabling higher pump intensity without the risk of grating damage. The measured waveforms are nearly single-cycle in reasonably good accordance with the result of numerical simulation, also shown in Figure 4-5. The absence of significant ringing on the trailing part can be an essential advantage when these pulses are used in particle acceleration setups [146]. The intensity spectra calculated from the measured and simulated waveforms can be seen in the inset of Figure 4-5. The simulated spectrum reaches its maximum at 0.38 THz. The spectral peaks of the measured THz pulses are at somewhat lower frequencies. The 0.3 – 0.4 THz mean frequency is suitable for particle acceleration applications.

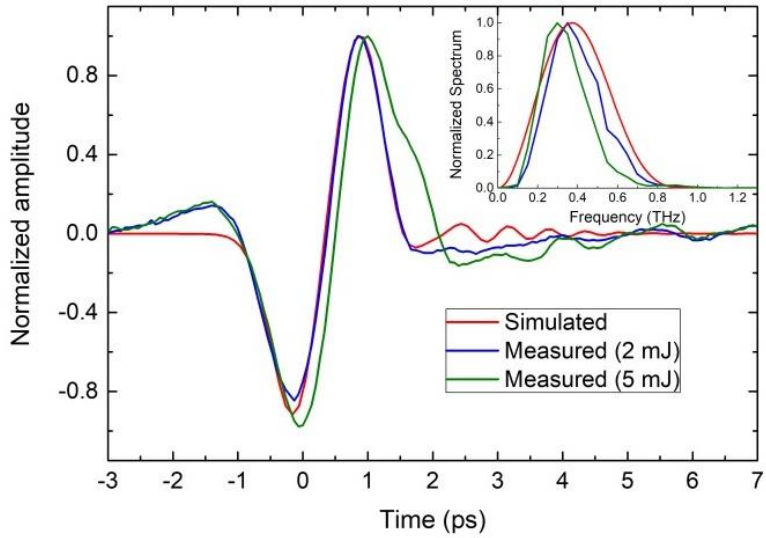

Figure 4-5 Measured (at two different pump pulse energies) and simulated THz pulse waveforms and their intensity spectra (inset).

Increasing the pump energy from 2 mJ to 5 mJ results in the appearance of a clear shoulder on the trailing part of the waveform and a shift of the spectral intensity maximum from 0.35 THz to 0.30 THz. Besides these changes, the saturation of efficiency can be observed. These observations are clear indications of nonlinear effects. Previously, nonlinear effects such as self-phase-modulation, cascading effect, combination of group-velocity-dispersion and angular dispersion, and stimulated Raman scattering were simulated in

conventional tilted-pulse-front pumped setups [63,147]. Another possible nonlinear effect is shifted current generation by the THz pulse, which was investigated in LN crystal, but not in the LN THz source [148]. Since the numerical model used in this work does not take into account these nonlinear effects, it can not explain the observed efficiency saturation and waveform and spectral distortions. However, the investigation of the nonlinear effects is less complicated for a plane-parallel crystal than for a prism-shaped LN crystal of 63° wedge angle and beyond of this work [149].

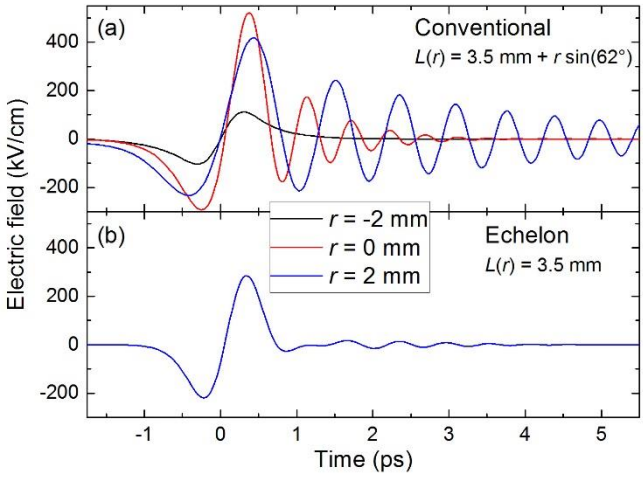

Figure 4-6 Calculated THz pulse waveforms at different positions across the THz beam for LN prism (a), and a plane-parallel LN slab (b). The lateral position in the input pump beam is labeled by r, where $r = 0$ corresponds to the beam center. $L(r)$ is the corresponding material length along the THz propagation direction [149].

Figure 4-6 illustrates the importance of a uniform interaction length across the pump and THz beams. The numerical simulation was done by co-authors in reference [149] for showing the characteristic of the LN slab. The output THz waveform strongly varies across the beam in a conventional prism-shaped LN crystal (Figure 4-6 (a)), the waveform can be nearly perfectly uniform in a plane-parallel LN slab with an echelon (Figure 4-6(b)). This feature is essential for a straightforward scalability to extremely high THz pulses energies by simply increasing the pump spot size and energy, as well as for producing the highest possible THz peak field strengths by the excellent focusability [149].

4.1.3. Conclusions

A net type of tilted-pulse-front pumped THz source has been demonstrated, which is based on a $LiNbO_3$ plane-parallel slab with an echelon structure on its input surface. Single-cycle pulses of 1.0 μJ energy and 0.30 THz central frequency have been generated with 5.1×10^{-4} efficiency with such a source. Estimation of the different factors influencing the efficiency, it was found

that one order-of-magnitude increase in efficiency could be expected by pumping a cryogenically cooled echelon of increased size and thickness with a Ti:sapphire laser.

4.2. Semiconductor multicycle THz pulse source

4.2.1. Calculation

The semiconductor nonlinear material selected for the simulations was GaP. Whereas other semiconductors are also suitable for multicycle THz pulse generation. GaP is preferred because of its relatively large direct (indirect) bandgap of 2.78 eV (2.27 eV). Its availability in larger sizes and better quality than, e.g. ZnTe, and its relatively small absorption and dispersion in the THz range. Furthermore, a small pulse-front tilt angle of about 20°-30° is needed for phase matching in optical rectification (Figure 4-7 (a)), resulting in only a minor variation of the duration of (sub-)ps-long pump pulses with propagation distance due to angular dispersion. A relatively large bandwidth is available for efficient THz generation, mainly limited by the drop of the nonlinear coefficient towards a minimum at about 8 THz [150]. These features make GaP an advantageous choice for (broadband-tunable) multicycle THz pulse generation. A possible implementation of the GaP multicycle THz source relies on the recently demonstrated contact-grating technology [106]. In such a scheme (Figure 4-7 (b)), the THz propagation distance is equal to the crystal length L and the pump with a pulse-front tilt angle γ propagates a distance of $L/\cos(\gamma)$.

Further material parameters of GaP used in the calculations were a high-frequency dielectric constant of $\varepsilon_\infty = 9.0$, an electron effective mass of $m_{\text{eff}} = 0.25 \times m_{\text{e}}$ (m_{e} is the electron mass), and an electron scattering time of $\tau_{\text{sc}} = 180$ fs. Optical refractive index data [151] and the dielectric function in the THz range [152] were taken from the literature.

For the simulations, the one-dimensional wave equation with nonlinear polarization has been solved in the spectral domain (see Eq. (1)-(5) in [60]). The simulation model took into account the variation of the pump pulse duration with propagation distance due to material and angular dispersions, the frequency-dependent absorption, and the refractive index in the THz range due to phonon resonances and free-carrier absorption, latter caused by multiphoton absorption of the pump. In case of calculations involving phase-matching frequencies higher than 1 THz, the dispersion of the effective second-order nonlinear susceptibility, $\chi^{(2)}$, was also taken into account [150]. The dependence of the nonlinear susceptibility on the THz frequency for GaP is shown in Figure 4-7 (a). At low frequencies, a value of $\chi^{(2)} = 2 \times d_{\text{eff}} = 2 \times 24.8$ pm/V was used [153].

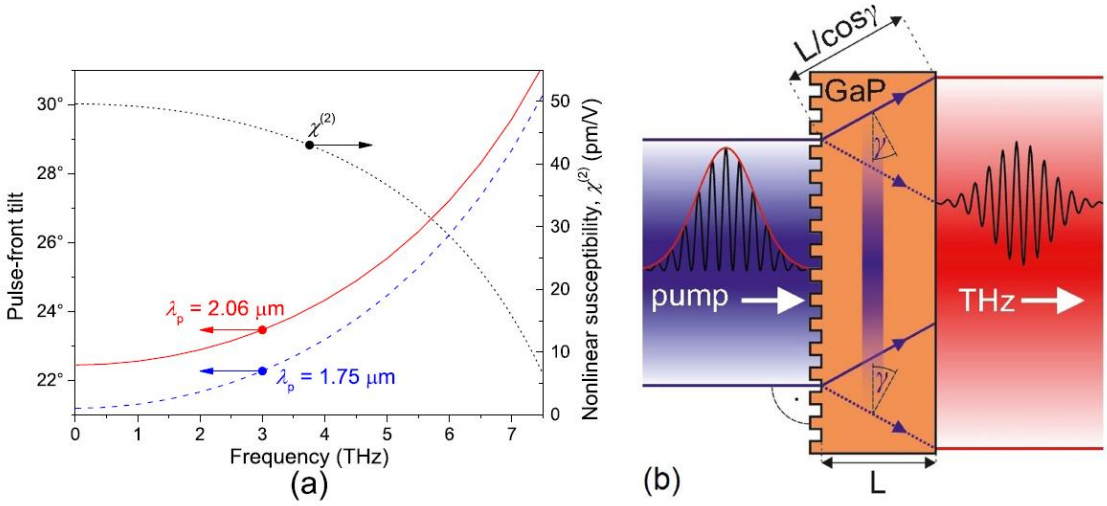

Figure 4-7. (a) Pulse-front tilt angle for 1.75 μm and 2.06 μm pump wavelengths (left vertical axis) and second-order nonlinear optical susceptibility (right vertical axis) in GaP as functions of the phase-matching THz frequency. (b) The geometry of the GaP contact-grating source pumped by an intensity-modulated pulse

Throughout the simulations, a central pump wavelength of $\lambda_p = 2.06$ μm was assumed. This is beyond the 1.33-μm cut-off wavelength for 3PA in GaP. Consequently, the lowest-order effective multiphoton absorption was 4PA. An estimation for the 4PA coefficient of ZnTe was taken from the reference, which is obtained by fitting simulation results to measured efficiency of THz generation pumped at 1.7 μm [108]. The 4PA coefficient for GaP will be investigated in more detail in the next chapter, but at the time of this simulation, it was not available yet. The ZnTe 4PA coefficient ($\beta_{4PA} = 3 \times 10^{-5}$ cm^5/GW^3) was used in the present work for GaP, which has similar bandgap to ZnTe. Higher-order multiphoton absorption effects were not taken into account, also in lack of available absorption coefficient data.

The contribution of the generated free carriers to the dielectric function at the THz angular frequency Ω was described by an oscillator term of zero resonance frequency $\varepsilon_\infty \omega_p^2/(\Omega^2 + i\,\Omega/\tau_{sc})$ (see e.g. [154]). The free-carrier plasma frequency is given by $\omega_p^2 = e^2 N_{fc}/(\varepsilon_0 \varepsilon_\infty m_{eff})$. The density of free carriers is given by $N_{fc} = \left(\beta_{4PA} \bar{I}_p^3/4\right) \cdot \bar{I}_p \sqrt{2\ln 2}\,\tau_p/\left(h\nu_p\right)$, whereby only 4PA was considered. An average pump intensity was considered with $\bar{I}_p = E_p/\left(\sqrt{2\ln 2}\,\tau_p w_p^2 \pi\right)$. We note that transient effects in free-carrier absorption were not taken into account in this model. In the above formulae, $-e$ is the electron charge, ε_0 is the electric permittivity of free space, τ_p is the pump pulse duration (full width at half maximum, of the intensity envelope, see also Figure 4-8 (a), h is Planck's constant, $\nu_p =$

c/λ_p is the pump central frequency, E_p is the pump pulse energy, and w_p is the pump beam radius (at $1/e^2$-value of the peak intensity).

Pump pulses with a constant intensity-modulation period were assumed, obtained by the superposition of two Gaussian pulses of equal amplitudes and pulse durations [155]. The small frequency offset between them was defining the desired THz frequency, where the appropriate pulse-front tilt angle set phase matching (Figure 4-7 (b)). For the sake of simplicity, unchirped pulses were considered. Throughout this work, THz pulse waveforms are referred to according to the number of electric field oscillation cycles within the full width at half maximum of their field envelope. A pulse comprising of at least two oscillation cycles is considered to be a multicycle pulse.

4.2.2. Results

According to Wynne and Carey [156], the THz waveform, in case of perfect phase matching, is given by the derivative of the pump pulse's intensity profile. In the case of multicycle THz pulses, this condition is fulfilled to a good approximation owing to the small relative bandwidth of the THz pulses. This enables a precise shaping of the THz waveform, as illustrated in Figure 4-8. The pulse length (see the intensity envelope in Figure 4-8 (a)) determines the bandwidth of each spectral band of the pump (Figure 4.7 (b)). In case of phase matching and negligible THz absorption, as a simple calculation of the nonlinear polarization for example with Gaussian pulses shows (see Eq. (3) in Ref. [60]), the THz bandwidth is $\sqrt{2}$ times larger than that of each pump band (Figure 4-8 (d)).

Numerical calculations were carried out in order to give guidelines for the design of multicycle THz sources using GaP as the nonlinear material for optical rectification. The frequency and waveform are given and the main parameters to be optimized are the crystal length and the pump intensity. The calculated pump-to-THz energy conversion efficiency as a function of the pump intensity is shown in Figure 4-9 for 1 THz phase-matching frequency and different crystal lengths of 3 mm, 5 mm, and 8 mm. For each length, the generation of three-, five-, and ten-cycle THz pulses was considered.

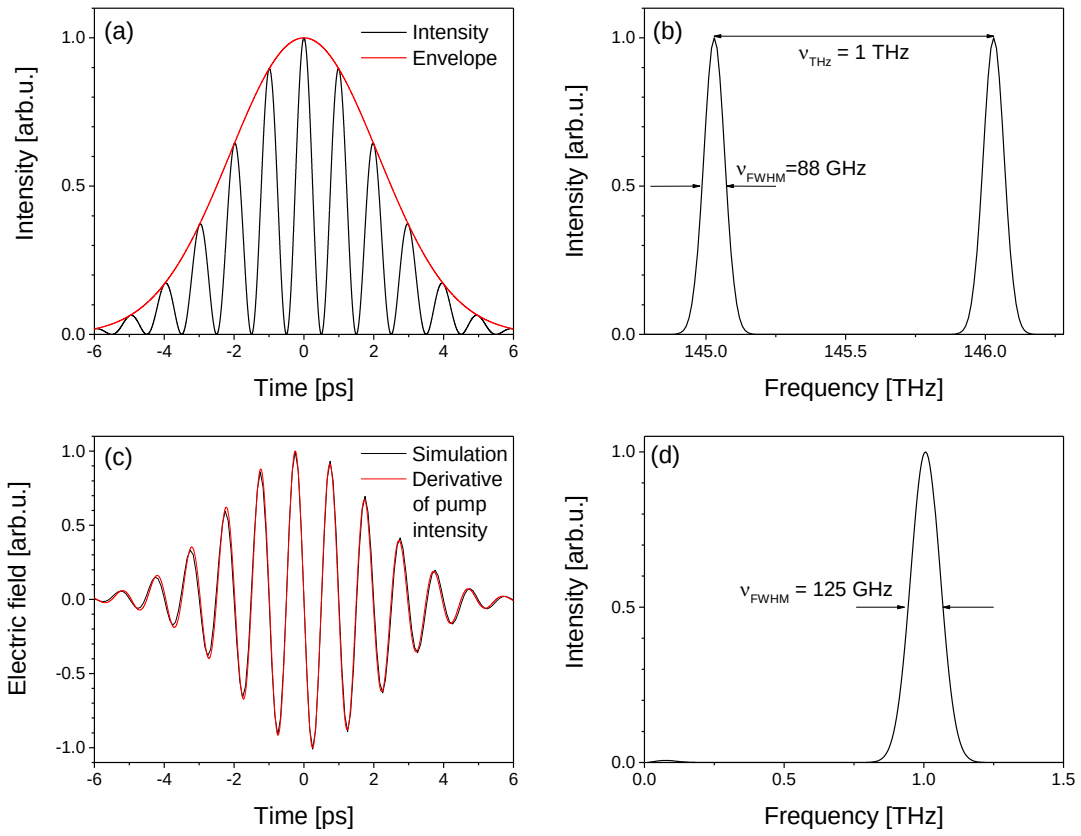

Figure 4-8. Example of multicycle THz pulse generation by intensity-modulated pump pulses. (a) Intensity-modulated pump pulse of 5 ps duration. (b) Spectrum of the shaped pump pulse. (c) The waveform of the generated multicycle THz pulse (solid black line) and the derivative of the pump intensity (red dashed line). (d) Spectrum of the THz pulse. The crystal length was 5 mm, and the pump peak intensity was 7.5 GW/cm^2. Phase matching was set at 1 THz.

A saturation regime follows the initial increase in efficiency with increasing pump intensity. For example, in the case of $L = 5$ mm crystal length, a maximum of the efficiency is reached at about 10 GW/cm^2 pump intensity for a 3-cycle pulse. At still higher intensities, the efficiency rapidly decreases. The reason for this behavior is the onset of 4PA of the pump and the resulting free-carrier absorption in the THz range. Similar behavior is observed for larger numbers of cycles. The maximum efficiencies vary from 0.20% (three cycles) to 0.14% (ten cycles). The efficiency is decreasing with an increasing number of cycles because of the increasing pump pulse duration and energy (at a constant pump intensity), resulting in a larger number of generated free carriers. A significant more than 5x increase in the efficiency maximum from 0.08% to 0.45% is observed as the crystal length is increased from 3 mm to 8 mm in case of three cycles. The increase is similar for five and ten cycles. Figure 4-10 shows the dependence of the THz peak electric field on the pump intensity for three-, five-, and ten-cycle THz pulses, 1 THz phase-matching frequency, and $L = 5$ mm crystal length. The

dependence is of similar character as that of the efficiency, with slightly shifted optimal intensities.

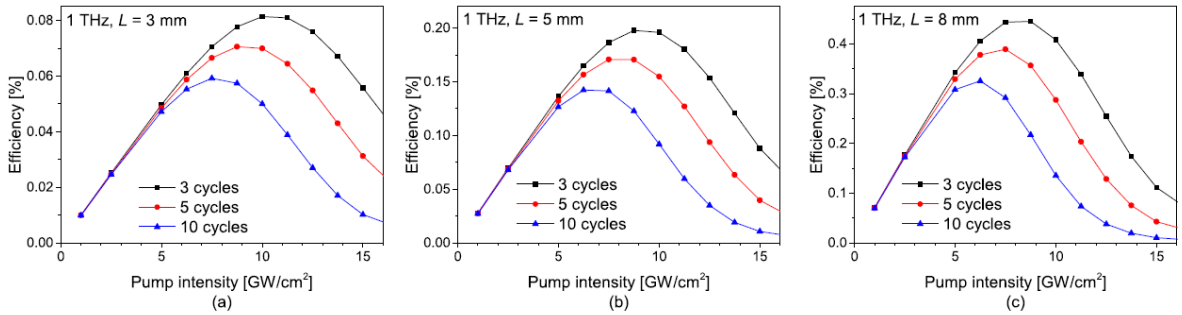

Figure 4-9. Calculated pump-to-THz energy conversion efficiency as a function of the pump intensity for three-, five-, and ten-cycle pulses, phase-matching at 1 THz frequency, and different crystal lengths of L = 3 mm (a), L = 5 mm (b), and L = 8 mm (c).

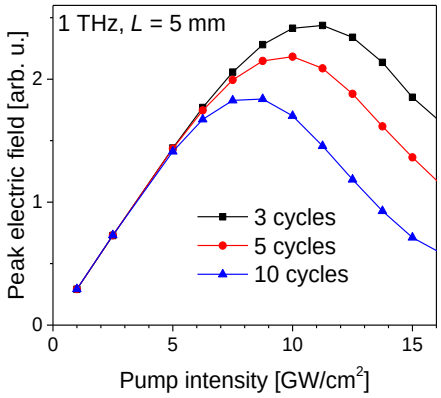

Figure 4-10. Calculated THz peak electric field as a function of the pump intensity for three-, five-, and ten-cycle

Figure 4-9 was indicating a favorable scaling of the THz generation efficiency with increasing crystal length. As good-quality GaP single crystals are available in relatively large sizes (of >2 cm lateral size). It is technically relevant to extend the investigations to more extensive crystal lengths, too. Figure 4-11 (a) shows the example of five-cycle pulse generation at 1 THz frequency. There is a difference as compared with Figure 4-9, where the efficiency maximum is around 10 GW/cm^2 pump intensity in the inside crystal. At this intensity, the efficiency increases up to about 0.5% over a crystal length of about 15 mm. The efficiency remains nearly constant over longer distances. Interestingly, the rate of efficiency growth with increasing crystal length is larger and the efficiency growth continues over larger distances at lower pump intensities of 7.5 GW/cm^2 and 5 GW/cm^2. Thus, an optimal combination of a low pump intensity of 5 GW/cm^2 and a large crystal length of 46 mm can enable a conversion efficiency as high as 7.7%. We note that such a large crystal block could also be realized by bonding a few thinner crystal blocks together, similarly to the sandwiched crystals often used

for electro-optic sampling. The reason for the favorable scaling of the efficiency with crystal length at low pump intensities is the significantly smaller free-carrier absorption.

In accordance with the favorable length scaling of the efficiency, a nearly linear increase of the peak electric field over a large crystal length of 46 mm is observed at 1 THz phase-matching frequency and a low pump intensity of 5 GW/cm^2, indicating a negligible role of absorption and dispersion (Figure 4-11 (c)). In contrast, at a higher pump intensity of 10 GW/cm^2, the nearly linear increase of the peak field strength is maintained only over less than 10 mm in length.

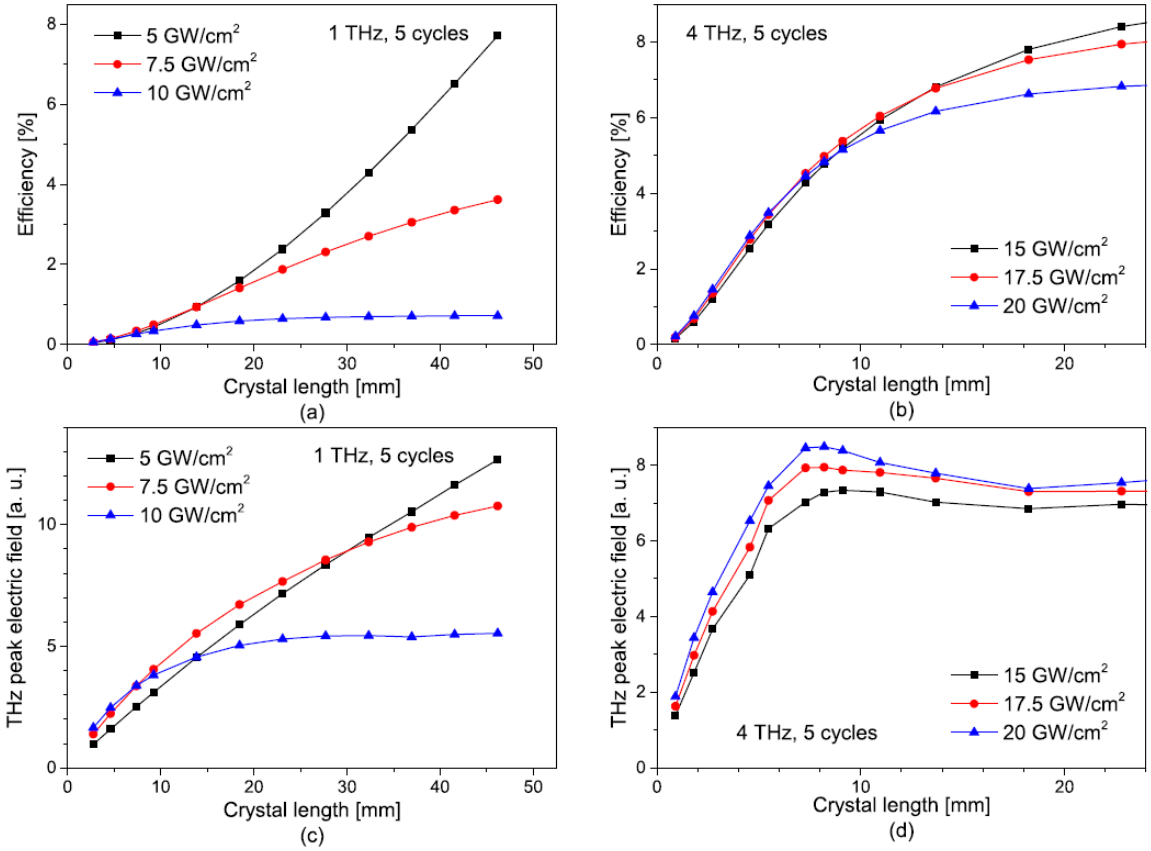

Figure 4-11. Conversion efficiency and peak electric field as functions of the crystal length in case of 5-cycle pulses at 1 THz (a, c), and 4 THz (b, d) phase-matching frequencies and various pump intensity levels.

As discussed in the previous work of our work [108], one important advantage of GaP is the possibility to extend THz generation by optical rectification to higher frequencies [157]. The transverse optical phonon frequency in GaP is at 11 THz [150]. When approaching the resonance from the low-frequency side, the second-order nonlinear coefficient decreases (see Figure 4-7 (b)), which prohibits efficient THz generation beyond about 7 THz [150]. Therefore, GaP can be suitable as a source of multicycle THz pulses in the 0.1 - 7 THz frequency range. This bandwidth is significantly larger than the useful bandwidth of ZnTe [108].

In order to explore the prospects of multicycle THz pulse generation at phase-matching frequencies higher than 1 THz. Carried out simulations, whereby the dispersion of the nonlinear susceptibility was taken into account. Figure 4-12 shows the calculated THz generation efficiency as a function of the pump intensity for different multicycle pulse frequencies of 2, 4, and 6 THz. The crystal length was 5 mm in all of these cases. The behavior at 2 THz is similar to that discussed above for 1 THz (Figure 4-9 (b)), except that now the peak efficiencies are about 6 times higher, reaching 1.1% (0.85%) for a three-cycle (ten-cycle) pulse for the higher optimal pump intensities of 10 - 15 GW/cm^2. The increase in efficiency continues for still higher frequencies of 4 THz (Figure 4-12 (b)), reaching 2.6% (3.5%) for a three-cycle (ten-cycle), whereby a larger number of cycles can be generated more efficiently. At the same time, one can observe a shift in the optimum intensities towards still higher values (17.5 to 22.5 GW/cm^2). The increasing efficiency with increasing phase-matching frequency can be explained by the favorable scaling of the optical rectification efficiency with the square of the frequency and by the higher optimal pump intensity. The latter is enabled by a decreasing free-carrier absorption coefficient. At an even higher frequency of 6 THz (Figure 4-12 (c)), the maximum achievable efficiencies reduced. The reason is the increased absorption of the material and the reduction of the nonlinear coefficient, both associated with the transverse optical phonon resonance.

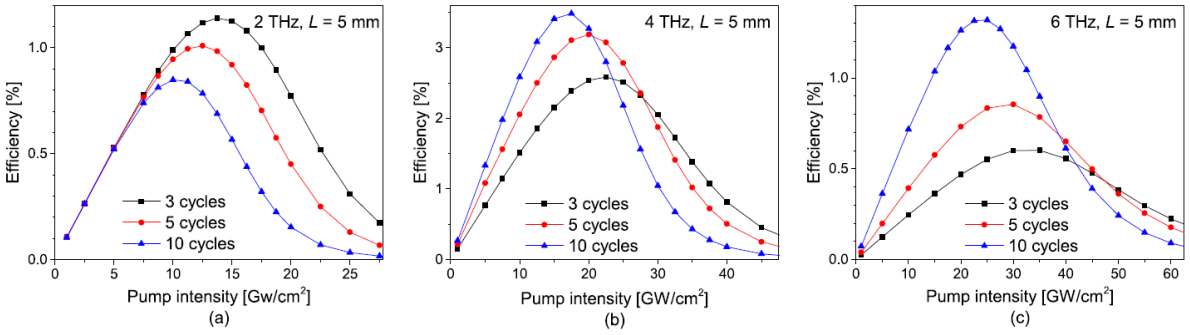

Figure 4-12. Calculated pump-to-THz energy conversion efficiency as a function of the pump intensity for three-, five-, and ten-cycle pulses, 5 mm crystal length, and different phase-matching frequencies of 2 THz (a), 4 THz (b), and 6 THz (c).

The scaling of the THz generation efficiency and the peak electric field with the crystal length is shown in Figure 4-11 (b) and Figure 4-11 (d), respectively, for the case of 4 THz phase matching frequency. For all three considered pump intensities, the efficiency increases up to about 6% to 7% at 15 mm crystal length, beyond which it saturates. The maximum peak field is approached already at 8 mm (Figure 4-11 (d)), beyond which even a moderate decrease

can be observed. The reason is the increased influence of material and plasma dispersion at such higher THz frequencies, which reduce the THz spectral width and lengthen the pulse.

The maximum predicted achievable THz generation efficiencies for three-, five-, and ten-cycle pulses at the respective optimal pump intensities and a crystal length of 5 mm are shown in Figure 4-13 as functions of the phase-matching THz frequency. The efficiencies increase up to their maxima in the range of 3.5 - 4.5 THz, with slightly different peak frequencies for the three-, five-, and ten-cycle cases. At still higher frequencies, the efficiency decreases due to phonon absorption and the reduction of the nonlinear coefficient, as mentioned above. These effects significantly reduce the achievable efficiency and limit the bandwidth to about 7 THz.

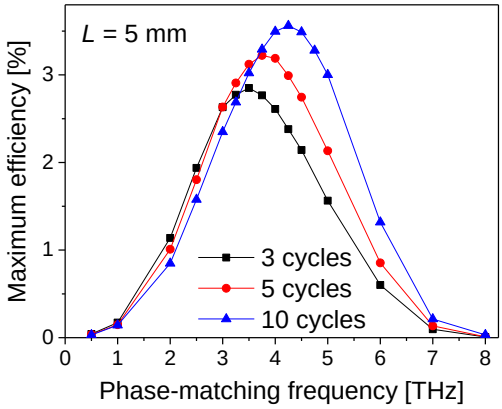

Figure 4-13. Maximum achievable THz generation efficiency for the respective optimal pump intensities as a function of the THz frequency, for three-, five-, and ten-cycle pulse generation. The crystal length was 5 mm in all cases.

4.2.3. Conclusion

Multicycle THz pulse generation by optical rectification in the semiconductor nonlinear material GaP was investigated with the help of numerical simulations. It was shown that GaP, in combination with flexible and efficient pump source technology, such as the dual-chirped optical parametric amplifier [155], and the contact grating technology [106] can be a highly efficient and versatile source of multicycle THz pulses in a broad range of waveforms and frequencies. Pump-to-THz energy conversion efficiencies up to about 3% were predicted for 5 mm crystal length. Based on this, producing multicycle THz pulses with about 1.2 mJ energy from a GaP contact-grating source of about 1 cm^2 area is feasible by using intensity-modulated pump pulses with 40 mJ energy from a dual-chirped optical parametric amplifier [155]. For an optimal combination of THz frequency, pump intensity, and crystal length, efficiencies as high as 8% can be expected. THz pulses with a desired waveform and fixed or broadband-tunable

carrier frequencies can be produced, covering the low- and significant part of the mid-frequency THz range up to about 7 THz.

4.3. Measurement of effective four-photon absorption in semiconductors

4.3.1. Experiment

Nonlinear transmission measurements of fs pulses have been carried out by using the Z-scan technique. The experimental setup is shown in Figure 4-14. Pump pulses of $\lambda_0 = 1.75$ μm central wavelength were delivered at 1 kHz repetition rate by a tunable optical parametric amplifier (Light Conversion, HE TOPAS), driven by a Ti:sapphire laser system (Coherent, Legend Duo). The full width at half maximum of the nearly Gaussian spectral intensity distribution of the pump pulses was about 51 nm. A set of dichroic long-pass filters have been used to suppress possible parasitic spectral components below about 1.65 μm. A pulse duration of 135 fs was measured by autocorrelation.

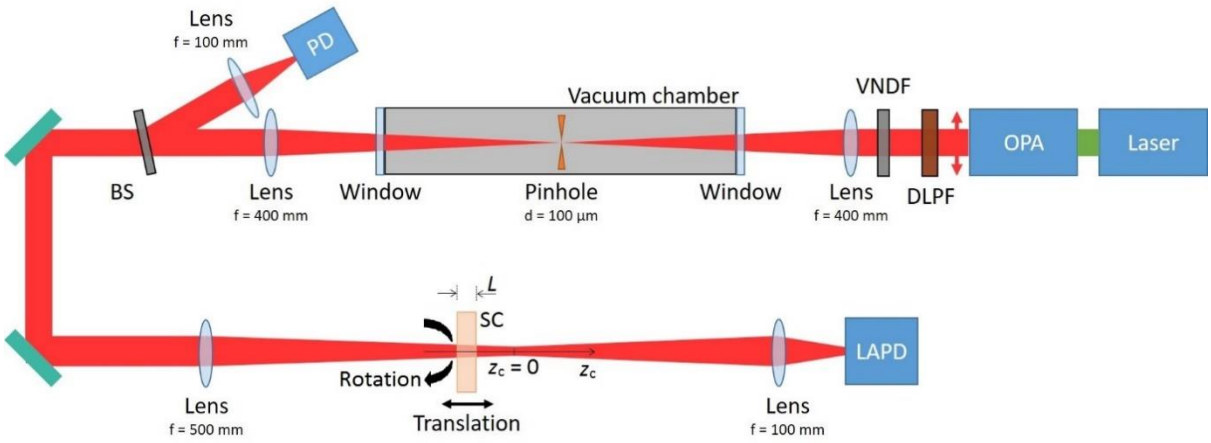

Figure 4-14. Scheme of the experimental setup. OPA: optical parametric amplifier, DLPF: dichroic long-pass filters, VNDF: variable neutral density filter, BS: beam splitter, PD: photodiode, SC crystal: semiconductor crystal, LAPD: large area photodiode.

A spatial filter was used to improve the pump beam quality to nearly Gaussian intensity profile and cylindrical symmetry. The spatial filter consisted of a pair of 400-mm focal-length lenses in a confocal arrangement, and a circular pinhole of 100 μm diameter, placed inside a vacuum chamber with two uncoated windows. A lens with 500 mm focal length was used to focus the beam for the Z-scan measurement. The knife-edge technique has carefully measured the horizontal and vertical beam profiles at several positions along the propagation direction of the focused beam. The absence of astigmatism has been verified in test Z-scan measurements, as well. The waist radius of the focused pump beam was $w_0 = 39$ μm (at $1/e^2$ of the peak intensity). The Rayleigh range was $2z_R = 5.5$ mm, significantly larger than the crystal length

L. The sample crystal was mounted on a motorized linear stage to move it along the beam propagation direction (z-axis) around the focus. A large-area Ge photodiode of 19.6 mm^2 sensitive area (Thorlabs DET50B/M) was used to measure the power transmitted through the sample. A lens with 100 mm focal length and 25 mm diameter, placed between the sample and the photodiode, was used to avoid closed-aperture effects in the Z-scan measurements.

The laser power transmitted through the sample crystal has been measured as a function of the crystal's z-position. Z-scan measurements with GaP and ZnTe crystals have been carried out at various pump energy levels. A step-variable neutral density filter (Thorlabs NDC-100S-4M) was used to attenuate the beam and regulate the pump intensity. In a second measurement series, the polarization direction of the linearly polarized pump pulses has been rotated in the plane of the GaP crystal by rotating the crystal about the beam axis.

Multiphoton absorption of the [110]-oriented GaP and ZnTe crystals of 10 mm × 10 mm size and $L = 1$ mm thickness have been measured at room temperature. The GaP crystals were purchased from two different manufacturers (Pi-Kem and Moltech); the ZnTe was from Moltech. Both GaP and ZnTe crystallize in the zincblende structure, $\bar{4}3m$. The (direct) bandgap energies (E_g) of GaP and ZnTe are 2.79 eV and 2.26 eV [154,158], respectively. In GaP, the smaller indirect bandgap of 2.27 eV has been found to play a less important role in multiphoton absorption induced by fs pump pulses [129,158,159], due to the smaller probability of the indirect transition than that of the direct one. The cut-off wavelength for 3PA, $\lambda_{cutoff} = 3hc/E_g$, is 1.33 μm for GaP and 1.65 μm for ZnTe. Here, h is the Planck constant and c is the speed of light in the vacuum. At pump wavelengths longer than the cut-off, interband linear absorption, 2PA, and 3PA are not effective in the respective material, but 4PA and higher-order multiphoton absorption can still be present. The 1.75 μm is chosen for the central pump wavelength ensured that the entire spectrum was located above the 3PA cut-off wavelength for both materials (for example, the spectral intensity at the 3PA cut-off in ZnTe was less than 2% of the peak intensity). The 4PA cut-off wavelength, $\lambda_{cutoff} = 4hc/E_g$, is 1.78 μm for GaP and 2.19 μm for ZnTe. In case of GaP, the long-wavelength wing of the pump spectrum containing about 10 % of the pulse energy was located beyond the 4PA cut-off.

4.3.2. Numerical model

A pulse propagation model in the slowly-varying envelope approximation was used, which included the effects of linear dispersion and 4PA inside the crystal. Diffraction and self-focusing effects have been neglected inside the crystal because relatively thin samples were

used in the experiment. In the calculations, a Gaussian pulse was assumed, both in time and space, incident onto the crystal. The intensity of the pulse just after entering the crystal was given by:

$$I(t, z = 0, \rho; z_c) = I_0 \frac{w_0^2}{w^2(z_c)} e^{-4\ln(2)\frac{t^2}{\tau^2}} e^{-\frac{2\rho^2}{w^2(z_c)}} \quad (34)$$

Here, t is the time, z ($0 \leq z \leq L$) is the coordinate along the pulse propagation direction inside the crystal, ρ is the radial coordinate, z_c is the coordinate of the input surface of the crystal in the Z-scan measurement with $z_c = 0$ corresponding to the focus. The radius at $1/e^2$ of maximum intensity of the Gaussian beam is $w(z_c)$, the waist radius is w_0, and the full width at half maximum pulse duration is τ. I_0 is the peak intensity (maximum in space and time) inside the crystal, taking into account Fresnel losses. The complex electric field envelope inside the crystal is related to the intensity as

$$A(t, z, \rho; z_c) = \sqrt{\frac{2I(t, z, \rho; z_c)}{\varepsilon_0 c n_0}}, \quad (35)$$

where ε_0 is the vacuum permittivity and n_0 is the refractive index of the crystal at the central frequency of the pulse.

The following equation gives the variation of the intensity due to 4PA:

$$\frac{\mathrm{d}}{\mathrm{d}z} I(t, z, \rho; z_c) = -\beta_4 I^4(t, z, \rho; z_c), \quad (36)$$

where β_4 is the 4PA coefficient. Therefore, the effect of 4PA on the field amplitude, an envelope is given by

$$\frac{d}{\mathrm{d}z} A(t, z, \rho; z_c) = -\frac{1}{16} \beta_4 (\varepsilon_0 c n_0)^3 A(t, z, \rho; z_c)^7. \quad (37)$$

By using a split-step Fourier method with Δz step size, linear dispersion was accounted for in the spectral domain in the moving frame of the pulse according to the following equation:

$$A(t, z + \Delta z, \rho; z_c) = \mathcal{F}^{-1}\left[\mathcal{F}[A(t, z, \rho; z_c)] e^{i\frac{[n(\omega) - n_g(\omega_0)]\omega}{c}\Delta z}\right]. \quad (38)$$

Here, $\mathcal{F}$ ($\mathcal{F}^{-1}$) denotes (inverse) Fourier transform, ω is the angular frequency, and $n_g(\omega_0)$ is the group refractive index of the crystal at the $\omega_0 = 2\pi c/\lambda_0$ the central frequency of the pulse.

Equations (37) and (38) were numerically solved for different radial coordinates ρ using a split-step Fourier method, similar to that in Ref. [160]. The Z-scan curve, i.e., the normalized transmission T through the sample crystal, as fa unction of the crystal position z_c can be obtained by

$$T(z_c) = \frac{\int_{-\infty}^{\infty}\int_{0}^{\infty}|A(t, z = L, \rho; z_c)|^2 \rho \mathrm{d}\rho \mathrm{d}t}{\int_{-\infty}^{\infty}\int_{0}^{\infty}|A(t, z = 0, \rho; z_c)|^2 \rho \mathrm{d}\rho \mathrm{d}t}, \quad (39)$$

4.3.3. Results

The results of open-aperture Z-scan measurements in [110]-cut GaP and ZnTe crystals, pumped at 1.75 μm wavelength, are shown in Figure 4-15. The normalized transmission value refers to those inside the crystal and has been corrected for the Fresnel loss. Negative (positive) z_c values refer to crystal positions before (behind) the focus at $z_c = 0$. In these measurements, the polarization of the pump pulse was either along the $[\bar{1}11]$-direction or along the $[1\bar{1}1]$-direction of the crystals. These directions correspond to the maxima of the second-order nonlinear polarization and are typically used for example in THz generation by optical rectification [106,107]. The intensity values given in the legends refer to peak intensities I_0 at the beam centre inside the sample materials.

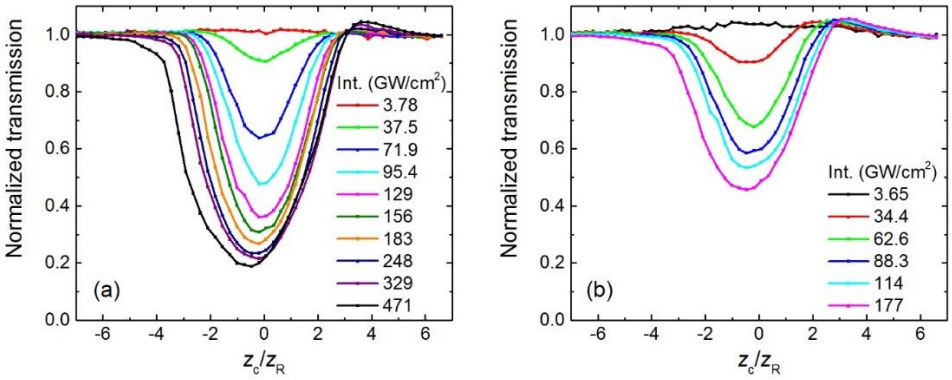

Figure 4-15. Measured Z-scan curves at various I_0 on-axis peak pump intensity levels for GaP (from Pi-Kem, a) and ZnTe (b).

In the case of GaP (Figure 4-15 (a)), the minimum of the measured relative transmission rapidly decreases with increasing pump intensity. At about 150 GW/cm^2, saturation of the nonlinear absorption sets on, indicating, besides 4PA, the contribution of other nonlinear effects at higher intensities. In this regime, one can also observe a forward shift of the transmission minima and a change of the shape of the Z-scan curves with increasing pump intensity. At the highest intensities (≳300 GW/cm^2), the Z-scan curves become asymmetric, which is the signature of closed-aperture effect and can also explain the forward shift of the

transmission minima. This was observable despite using an additional positive lens before the detector (see Figure 4-14). In the case of ZnTe Figure 4-15 (b)), similar behaviour can been observed, except that nonlinear change of the transmission is somewhat smaller at comparable intensities and the saturation effects become visible below 100 GW/cm^2.

In order to filter out closed-aperture effect at high intensities, the measured Z-scan curves have been symmetrized according to $T_s(z_c) = [T(z_c) + T(-z_c)]/2$ [161]. The minima of the measured and symmetrized Z-scan curves have been fitted by varying the 4PA coefficient in the nonlinear pulse propagation model described before. In each case, a few measured data points with the lowest transmission values were considered for fitting by the least-square method. The only free parameter in the fitting was the β_4 coefficient. Examples of measured and symmetrized GaP Z-scan curves, corresponding to different peak pump intensities are shown in Figure 4-16, together with the calculated curves, using the best-fit 4PA coefficient value. The measured and the calculated Z-scan curves are in good agreement in the intensity regime below about 100 GW/cm^2, where no saturation of the nonlinear transmission occurs (Figure 4-16 (a)). With the onset of saturation (Figure 4-16 (b)) and closed-aperture effects (Figure 4-16 (c)), the agreement is gradually reduced. The obtained 4PA coefficients are dependent on the peak pump intensity, which is consistent with the presence of other nonlinear effects besides 4PA. We note that considering the obtained intensity dependence of the 4PA coefficient in calculating the individual Z-scan curves could improve the agreement between experimental and calculated Z-scan curves. However, this adds significant numerical complexity to the model but does not change the 4PA values as they correspond to measured transmission minima. For this reason, such a correction has not been carried out here.

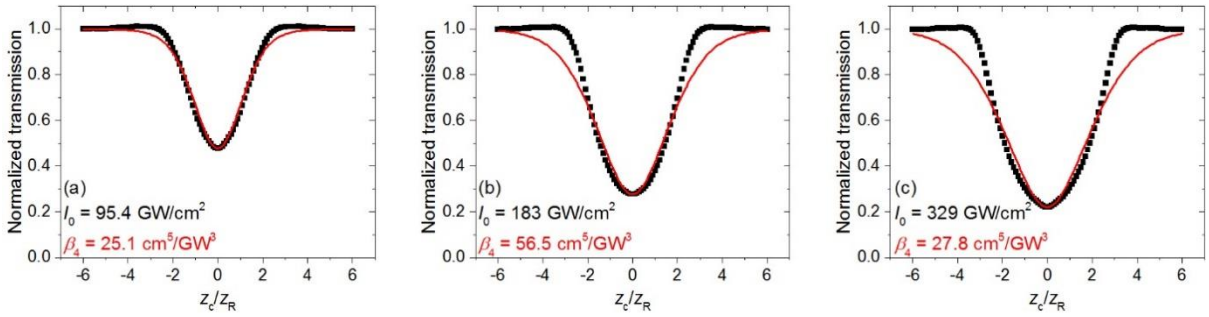

Figure 4-16. Examples of symmetrized Z-scan curves, measured at different I_0 on-axis peak pump intensities (symbols), and the best-fit calculated curves (solid line) in the case of GaP.

The intensity-dependent 4PA coefficients, obtained from fitting the measured-symmetrized Z-scan curves, are shown in Figure 4-17 as function of the on-axis peak pump intensity. In the case of GaP, the 4PA coefficient increases monotonically from 2.6×10^{-4}

cm^5/GW^3 at 37.5 GW/cm^2 pump intensity to its maximum of 56.5×10^{-4} cm^5/GW^3 at 183 GW/cm^2 intensity. The maximum is 64.9×10^{-4} cm^5/GW^3, in the case of the Moltech GaP crystal. The maximum is followed by a monotonic decrease at still higher intensities. There was no significant difference between the two GaP crystals. Similar behavior was found for ZnTe, but the maximum value of the 4PA coefficient was about six times smaller, measured at about three times lower intensity. The 4PA coefficient increases from 3.8×10^{-4} cm^5/GW^3 at 34.4 GW/cm^2 intensity to 9.7×10^{-4} cm^5/GW^3 at about 63 GW/cm^2. At higher intensities, the 4PA coefficient decreases.

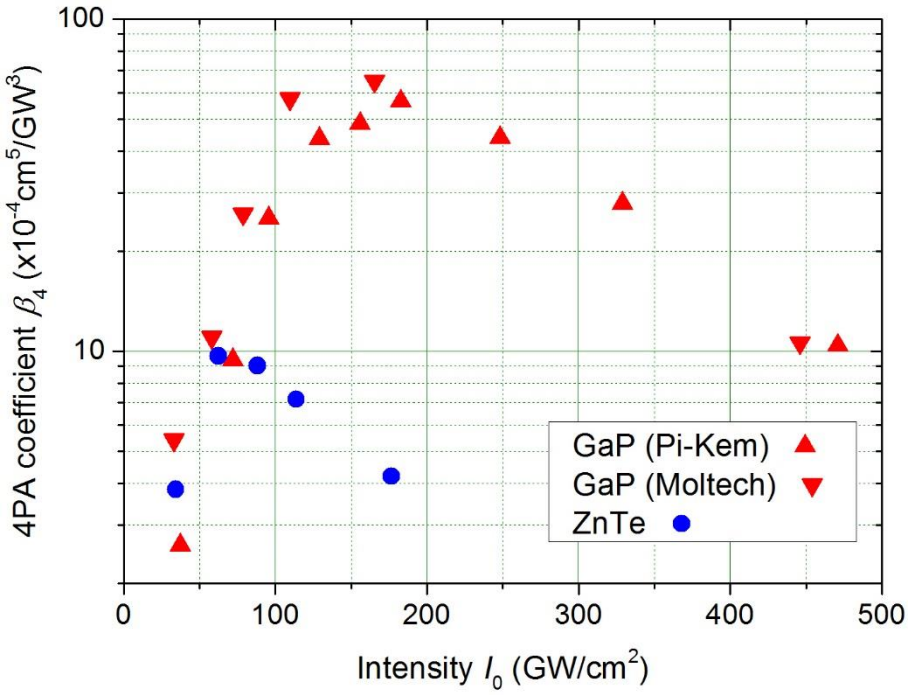

Figure 4-17. Intensity-dependent 4PA coefficients as function of the on-axis peak pump intensity.

The intensity dependence of the determined 4PA coefficients and the occurrence of closed-aperture effect at higher intensities, hinting to strong beam reshaping by nonlinear phase shift, are signatures of additional nonlinear effects not considered in the model. These effects may contribute both to nonlinear absorption as well as the nonlinear refractive index. Nonlinear absorption can be caused by several effects, such as five-photon and higher-order multiphoton absorption, the absorption of free carriers generated by multiphoton absorption, and tunnel ionization from the valence to the conduction band [127,162], or non-phase-matched second-harmonic generation and eventually subsequent 2PA. Contribution to the nonlinear phase can arise from the nonlinear refractive index n_2 and from free carriers generated by the effects mentioned above [163]. The nonlinear phase can also change the beam size, besides changing

the temporal shape, which can lead to the change of the free-space propagation of the beam, but also the change of the intensity and the nonlinear absorption within the sample.

Non-phase-matched second-harmonic generation, followed by 2PA is estimated to be less likely to contribute. Free-carrier generation by 4PA and its contribution to the nonlinear absorption was estimated to become significant at about 200 GW/cm^2 intensity. The highest intensity used in the case of GaP was 471 GW/cm^2, which gives a Keldysh parameter of about 3.2, indicating the absence of strong tunneling effects. Furthermore, a significant redistribution of the electron population due to the intense excitation can even lead to an additional chance of the linear and nonlinear optical parameters, and other material parameters, such as the bandgap. Further experimental and theoretical investigations are needed to clarify possible contributions of the mentioned effects. Such studies, which are beyond the scope of this work, may include the development of more sophisticated theoretical models and optical pump—THz probe measurements of transient carrier dynamics.

4PA can be a significant efficiency-limiting effect in semiconductor THz sources pumped at a wavelength longer than the cut-off for 3PA. The estimation of $(3 \pm 1) \times 10^{-5}$cm^5/GW^3 for the 4PA coefficient in ZnTe was obtained by fitting simulation results to experimental data on THz generation efficiency [108]. Simulations using this value of the 4PA coefficient agreed well with the observed saturation of the THz generation efficiency and the maximum efficiency found at 14 GW/cm^2 pump intensity. However, it is about one order of magnitude smaller than the smallest 4PA coefficient measured here by Z-scan at about two times higher intensity (Figure 4-17).

In a further Z-scan measurement series, the polarization direction of the linearly polarized pump pulses has been varied with respect to the dielectric Z[001]-axis of the [110]-oriented GaP crystal. The pump intensity was 65 GW/cm^2. The results, shown in Figure 4-18, clearly reveal the anisotropy of the 4PA coefficient, which varies between 3.8×10^{-4} cm^5/GW^3 and 15.6×10^{-4} cm^5/GW^3. The two largest values can be seen at 55° and 135° polarization angles, measured from the Z-axis. No polarization-dependent Z-scan measurements have been carried out with ZnTe here, but a similar behavior can be expected due to symmetry reasons. We note that the second-order nonlinear susceptibility, responsible for second harmonic generation or optical rectification, also exhibits a qualitatively similar anisotropy (see the empty red symbols and the red dashed curve in Figure 4-18 for second harmonic generation (SHG) GaP, and the Supplementary Material in Ref. [106] for ZnTe). Its maxima are at 54.7^0 and 125^0 (vertical

dashed lines in Figure 4-18), which are close to the 55^0 and 135^0 angles where 4PA maxima were found.

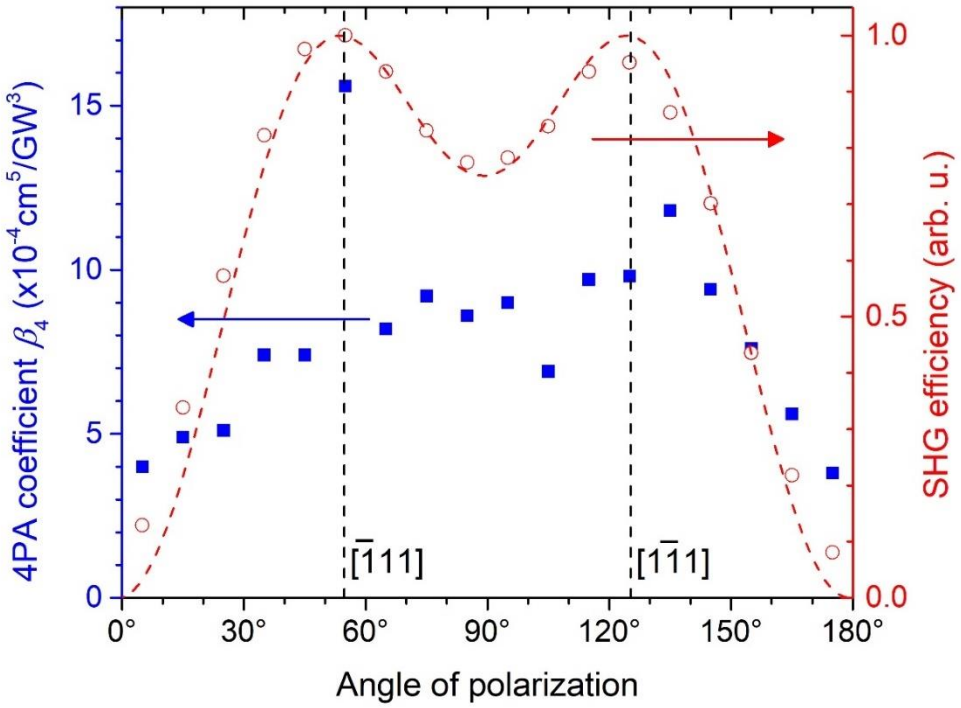

Figure 4-18. Measured anisotropy of the 4PA coefficient in GaP (full symbols, left vertical axis) as a function of the pump polarization angle. The measured (empty red symbols) and calculated (dashed red line) SHG efficiency (right vertical axis) is also shown. The vertical dashed lines indicate the given crystallographic directions.

The qualitatively similar anisotropy has been reported for 2PA [131] and 3PA [132] in [110]-oriented GaAs, which has the same symmetry group as GaP and ZnTe. Good agreement was found between 2PA anisotropy measurements of GaAs with ps [131] and ns [130] pulses. In the latter case, 2PA-induced free-carrier absorption was large, and the 2PA anisotropy was found to reflect the anisotropy of the band structure. An expression for the pump polarization dependence of the effective third-order nonlinear susceptibility, relevant for 2PA, can be easily derived from the tensor symmetry properties [131,164]. The description of 3PA anisotropy requires the knowledge of the symmetry properties of the fifth-order nonlinear susceptibility tensor, which is already sparse in the literature [165,166]. 4PA anisotropy requires to deal with the seventh-order nonlinear susceptibility tensor (of rank 8), which we have not found in the literature. Due to the uncertainties in the exact physical origin and the mathematical complexity, a theoretical discussion of 4PA anisotropy is beyond the scope of this work.

The estimation of 10^{-7} cm^5/GW^3 has been given for the 4PA coefficient of $LiNbO_3$ based on THz generation results with 1.03 μm pump wavelength [126]. This value is less reliable, as

it is dependent on another fitting parameter [126]. The values obtained in the present work for GaP and ZnTe are about three orders of magnitude larger. Despite uncertainties, such large difference underlines the importance of the knowledge of the 4PA coefficients in semiconductors, as 4PA can be relevant even at moderate optical intensities.

4.3.4. Conclusions

Intensity-dependent 4PA coefficients in GaP and ZnTe semiconductors have been measured by the Z-scan method using pump pulses of 1.75 μm wavelength and 135 fs duration. The choice of the pump wavelength longer than the cut-off for 4PA ensured that no interband linear, as well as two-and three-photon absorptions had to be taken into account. The intensity-dependent 4PA coefficients, obtained in an extensive range of pump intensities from about 30 GW/cm^2 up to about 500 GW/cm^2, vary from 2.6×10^{-4} to 65×10^{-4} cm^5/GW^3 in GaP, and from 3.8×10^{-4} to 9.7×10^{-4} cm^5/GW^3 in ZnTe. The anisotropy in 4PA has been shown in GaP.

5. THESIS STATEMENTS

1. A new type of tilted-pulse-front pumped THz source based on a $LiNbO_3$ plane-parallel slab with an echelon structure on its input surface was demonstrated [149]. Single-cycle pulses of 1.0 μJ energy and 0.30 THz central frequency were generated at 5.1×10^{-4} efficiency. One order-of-magnitude increase in efficiency is expected by pumping a cryogenically cooled echelon of increased size and thickness with a Ti:sapphire laser.

   This new scheme enables straightforward scaling to high THz pulse energies by increasing the lateral size and the pump pulse energy and focusing to extremely high field strengths. The pump pulse duration, the THz absorption and dispersion, and nonlinear effects are highly uniform across the THz beam profile in such a setup. This enables to produce symmetric THz beam with uniform pulse shape for excellent focusability and extremely high field strength. Further improvement and simplification of the setup are possible without using imaging.
2. Multicycle THz pulse generation by optical rectification in the semiconductor nonlinear material GaP was investigated with the help of numerical simulations. In the range of 0.1–7 THz frequency, pump-to-THz energy conversion efficiencies up to 3% was predicted for 5 mm crystal length. For an optimal combination of THz frequency, pump intensity, and crystal length, efficiencies as high as 8% of multicycle THz pulses can be expected [139]. Based on this, producing multicycle THz pulses with about 1.2 mJ energy from GaP contact grating source of about 1 cm^2 area is feasible by using intensity-modulated pump pulses with 40 mJ energy from a dual-chirped optical parametric amplifier.
3. Intensity-dependent effective 4PA coefficients in GaP and ZnTe semiconductors were measured by the Z-scan method using pump pulses of 1.75 μm wavelength and 135 fs duration. The 4PA coefficients vary from 2.6×10^{-4} to 65×10^{-4} cm^5/GW^3 in GaP, and from 3.8×10^{-4} to 9.7×10^{-4} cm^5/GW^3 in ZnTe. The anisotropy in 4PA was shown in GaP. The knowledge of the intensity-dependent 4PA coefficients is essential for the design of practical devices, such as efficient semiconductor THz sources [167,168].

6. ÖSSZEFOGLALÓ

A THz-es impulzusok felhasználási köre jelentősen növekedett a közelmúltban, köszönhetően a THz-es tudományban végbemenő fejlesztéseknek. Az impulzusok megnövekedett energiája és különleges tulajdonságai lehetőséget biztosítanak a THz-es impulzusok széles körű alkalmazására. Azonban, annak érdekében, hogy az új igényeknek meg lehessen felelni, folyamatosan új THz-es források fejlesztésére van szükség. Jelen dolgozat célja az intenzív THz-es impulzusok fejlesztése annak érdekében, hogy egyszerű, könnyen megvalósítható forrásokat hozzunk létre, amelyek nagy energiával és szabályozható impulzusparaméterekkel rendelkeznek. Munkámba lítium-niobát (LN) és félvezető nemlineáris optikai kristályokon alapuló új THz-es források numerikus szimulációjával és kísérleti vizsgálatával foglalkoztam.

Tézispontok:

I. Demonstráltam egy új típusú, lépcsős rács alakú (echelon) bemenő felülettel rendelkező plán paralel $LiNbO_3$ kristályt alkalmazó döntött-impulzusfronttal pumpált THz-es forrást [149]. A kísérlet során, egyciklusú, 1,0 µJ energiájú és 0,30 THz központi frekvenciájú impulzusokat $5{,}1 \times 10^{-4}$ hatásfokkal állítottam elő. Egy nagyságrenddel nagyobb növekedés várható, ha a megnövelt méretű és vastagságú kriogén módon hűtött echelon struktúrát Ti:sapphire lézerrel pumpáljuk.

   Ez az új elrendezés lehetővé teszi a THz-es impulzusok energiájának felskálázását a kristály méretének és a pumpa lézer energiájának növelésével, valamint extrém nagy térerősségek elérését fókuszálással. Ebben az összeállításban a pumpa impulzus impulzushossza, a THz abszorpciója és diszperciója, valamint a nemlineáris hatások egyformák a THz-es nyaláb keresztmetszete mentén. Az elrendezés lehető teszi szimmetrikus THz-es impulzusok előállítását a kiváló fókuszálhatóság és rendkívül magas térerősség érdekében. Az elrendezés továbbfejlesztése és egyszerűsítése lehetséges a leképezés elhagyásával.

II. Numerikus szimulációkkal többciklusú THz-es impulzusok generálását vizsgáltam optikai egyenirányítással GaP félvezetőben. A szimulációk a 0,1–7 THz frekvenciatartományon 3% pumpa-THz energiakonverziós hatásfokot jósolnak 5 mm-es kristály használatánál. A THz frekvencia, pumpa intenzitás és kristályhossz optimális megválasztása esetén a keletkező többciklusú THz impulzus hatásfoka % is lehet [139]. Ez alapján, 1,2 mJ energiával rendelkező többciklusos THz-impulzus állítható elő körülbelül 1 cm^2 területű GaP kontaktrácsban 40 mJ energiájú dual-chirped

optikai parametrikus erősítőből származó intenzitás-modulált pumpa impulzus felhasználásával.

III. Intenzitásfüggő 4PA koefficienseket mértem GaP és ZnTe félvezetőkben Z-scan módszerrel 1,75 um hullámhosszú és 135 fs impulzushosszú pumpa impulzusokat alkalmazva. Vizsgálataim szerint a 4PA együtthatók GaP-ban 2.6×10^{-4} és 65×10^{-4} cm^5/GW^3 között, ZnTe-ban pedig 3.8×10^{-4} és 9.7×10^{-4} cm^5/GW^3 között változnak. Kimutattuk a 4PA anizotrópiát GaP-ban. Az intenzitástól függő 4PA együtthatók ismerete elengedhetetlen az olyan gyakorlati eszközök tervezéséhez, mint amilyenek például a hatékony félvezető THz-források [167,168].

7. SUMMARY

7.1. Background and objectives

The study and control of materials with powerful THz fields [91,169] or the acceleration and manipulation of electrons [92] and protons [93] are emerging applications that require THz sources with unprecedented parameters. Besides the pulse energy, an excellent focusability is also essential to achieve the highest possible field strengths.

Optical rectification of ultrashort laser pulses with tilted pulse front in lithium niobate (LN) [170] has become a standard technique for efficient THz generation. Conventionally, a prism-shaped LN crystal, is used with a large wedge angle equal to the pulse-front tilt (63°). Such a source geometry results in a non-uniform pump propagation length across the beam, which can lead to a spatially varying interaction length for THz generation [60]. This negatively affects the THz beam quality and, consequently, the focusability, thereby limiting the achievable field strength. Lateral beam (and eventually waveform) nonuniformity is especially problematic in high-energy THz sources [171], where a large-diameter pump beam is needed.

Different approaches were proposed to mitigate the limitations of tilted-pulse-front pumped THz sources. Recently, a modified hybrid approach to provide uniform interaction length across large pump and THz beams were proposed [69]. The setup uses a plane-parallel LN slab as the nonlinear medium, which is equipped with an echelon structure on its input surface. Inside the LN slab, a segmented tilted pulse front is formed with an average tilt angle as required by phase matching.

Intense nearly single-cycle terahertz (THz) pulses can be used in materials science [91] and for the acceleration of electrons [92] and protons [93,94]. The waveguide and resonator structures proposed for electron acceleration can be even more efficiently driven by multicycle THz pulses. Multicycle THz pulses also could be used as drivers of coherent X-ray generation [96] and electron beam diagnostics. Multicycle narrowband THz pulses with lower peak amplitude, but higher spectral brightness may serve as a way of circumvent such electronic responses and still maintain high exciting strength for resonant driving in particular electronic, lattice, or magnetic nonlinear responses [97].

It was recently demonstrated that nonlinear semiconductor materials offer a promising alternative with scalability to highest THz pulse energies and field strengths [40,105-108], also enabling the construction of monolithic contact-grating sources [106]. Lee et al. showed the generation of multicycle narrow-bandwidth THz pulses in periodically inverted GaAs structures using optical rectification at 2 μm wavelength [109].

Semiconductor materials have been playing an essential role in many photonics-based technologies for decades. Novel high-power ultrashort-pulse laser and parametric sources, operating at infrared wavelengths, have recently enabled new application areas in nonlinear optics [124,125]. To design and optimize setups and devices utilizing intense optical driving of semiconductors, the knowledge of their nonlinear optical parameters, such as the nonlinear refractive index or multiphoton absorption coefficients, is very important.

Theoretical scaling laws for multiphoton absorption coefficients were given for direct-bandgap semiconductors based on a two-band model [128]. An early summary of theoretical models and experimental values of two- (2PA) and three-photon absorption (3PA) coefficients for a few selected materials can be found in Ref. [129]. The most commonly used method to measure 2PA and 3PA coefficients is the Z-scan technique [119]. This has been applied to measure the tensor properties (anisotropy) [133], by using the three nonlinear eigenpolarizations [134], and the dispersion of third-order nonlinearities (2PA) [133,135] in various semiconductors. The dispersion and the anisotropy of 2PA and 3PA in GaAs have been measured in the 1.3–2.5 μm wavelength range by 100-fs pulses [132]. A maximum in the 3PA coefficient has been found both in theory and experiment near the 3PA cut-off wavelength. In contrast, little is known about the four-photon absorption (4PA) and nonlinearities of even higher-order in semiconductors and other important optical materials. This knowledge can be crucial for applications driven by infrared pulses. For example, in the newly developed very perspective semiconductor THz generators, 4PA can be a significant limitation and hence should be considered in device design [108,139]. A first attempt to estimate the 4PA coefficient in ZnTe has been made based on THz generation results [108], but this approach is very indirect and therefore subject to uncertainties. GaP is another semiconductor nonlinear material of high interest for efficient THz generation [108,139], but no experimental data on its 4PA coefficient are available. Thus, there is a clearly perceived lack of knowledge on important material data.

7.2. Methods

The investigated hybrid-type setup is a combination of the conventional scheme, containing a diffraction grating and imaging optics, and a nonlinear material with an echelon profile on its entrance surface (nonlinear echelon slab, (NLES), Figure 7-1). Pump pulses of 200 fs pulse duration and 1030 nm central wavelength were delivered by a cryogenically cooled Yb:CaF2 regenerative amplifier operating at 1 kHz repetition rate. Up to about 2.5 mJ pump pulse energy was used in the experiment. At the pump wavelength used and at room temperature, a pulse front tilt of about 63° is required for phase matching in LN. In the case of the NLES, this pulse

front tilt angle needs to be produced in the air at the entrance of the crystal. Here, $n_g = 2.215$ is the group index of LN at the 1030 nm pump wavelength.

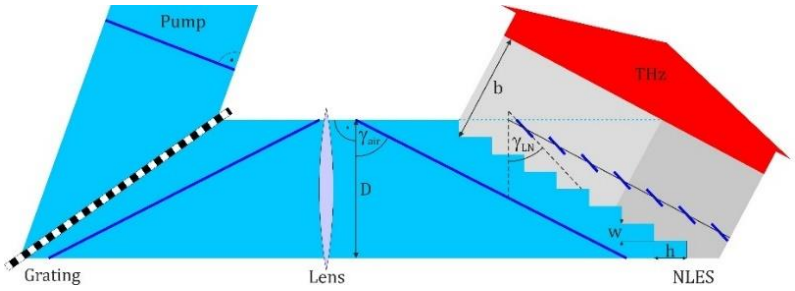

Figure 7-1. Scheme of NLES experimental setup.

For the simulations, multicycle THz pulses, the one-dimensional wave equation with the nonlinear polarization has been solved in the spectral domain (see Eq. (1)-(5) in [60]). The simulation model took into account the variation of the pump pulse duration with propagation distance due to material and angular dispersions, the frequency-dependent absorption and the refractive index in the THz range due to phonon resonances and FCA, latter caused by MPA of the pump. In case of calculations involving phase-matching frequencies higher than 1 THz, the dispersion of the effective second-order nonlinear susceptibility, $\chi^{(2)}$, was also taken into account [150].

The semiconductor nonlinear material selected for the simulations was GaP. GaP is preferred here because of its relatively large direct (indirect) bandgap of 2.78 eV (2.27 eV), its availability in larger sizes and better quality than, e.g., ZnTe, and the relatively small absorption and dispersion in the THz range. Furthermore, a small pulse-front tilt angle of about 20°-30° is needed for phase matching in optical rectification, resulting in only a minor variation of the duration of (sub-)ps-long pump pulses with propagation distance due to angular dispersion.

Nonlinear transmission measurements with fs pulses have been carried out by using the Z-scan technique. The experimental setup is shown in Figure 7-2. Pump pulses of $\lambda_0 = 1.75$ μm central wavelength were delivered at 1 kHz repetition rate by a tunable optical parametric amplifier, driven by a Ti:sapphire laser system. The full width at half maximum of the nearly Gaussian spectral intensity distribution of the pump pulses was about 51 nm. A set of dichroic long-pass filters have been used to suppress possible parasitic spectral components below about 1.65 μm. A pulse duration of 135 fs was measured by autocorrelation.

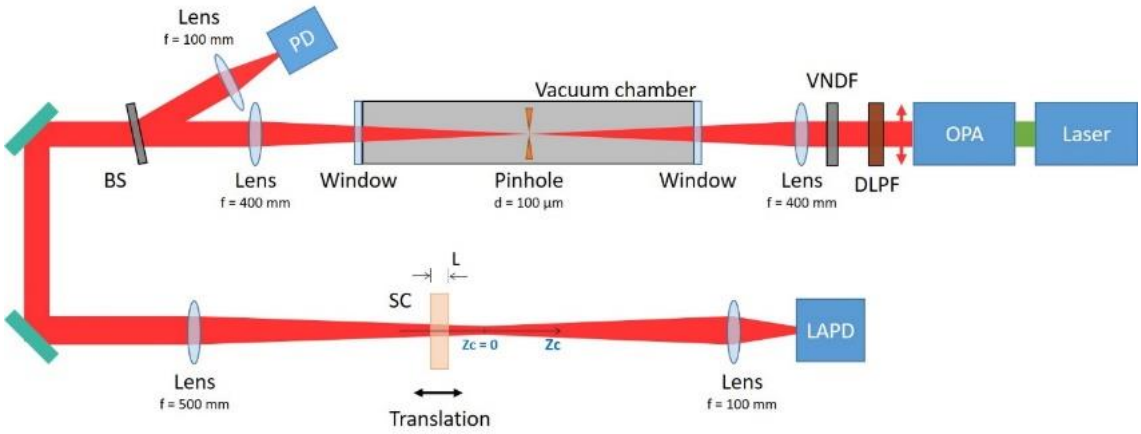

Figure 7-2. Scheme of Z-scan measurement setup.

A spatial filter was used to ensure a pump beam of good quality, with nearly Gaussian intensity profile and cylindrical symmetry. A lens with 500 mm focal length was used to focus the beam for the Z-scan measurement. The knife-edge technique has carefully measured the horizontal and vertical beam profiles at several positions along the propagation direction of the focused beam. The waist radius of the focused pump beam was $w_0 = 39$ µm (at $1/e^2$ of the peak intensity). The Rayleigh range was $2z_R = 5.5$ mm, significantly larger than the crystal length L. The sample crystal was mounted on a motorized linear stage to move it along the beam propagation direction (z-axis) around the focus. A large-area Ge photodiode was used to measure the power transmitted through the sample.

7.3. New scientific achievement

I. A new type of tilted-pulse-front pumped THz source based on a $LiNbO_3$ plane-parallel slab with an echelon structure on its input surface was demonstrated [149]. Single-cycle pulses of 1.0 µJ energy and 0.30 THz central frequency were generated at 5.1×10^{-4} efficiency. One order-of-magnitude increase in efficiency is expected by pumping a cryogenically cooled echelon of increased size and thickness with a TiLsapphire laser. This new scheme enables straightforward scaling to high THz pulse energies by increasing the lateral size and the pump pulse energy and focusing to extremely high field strengths.

II. Multicycle THz pulse generation by optical rectification in the semiconductor nonlinear material GaP was investigated with the help of numerical simulations. In the range of 0.1–7 THz frequency, pump-to-THz energy conversion efficiencies up to 3% was predicted for 5 mm crystal length. For an optimal combination of THz frequency, pump

intensity, and crystal length, efficiencies as high as 8% of multicycle THz pulses can be expected [139].

III. Intensity-dependent effective 4PA coefficients in GaP and ZnTe semiconductors were measured by the Z-scan method using pump pulses of 1.75 μm wavelength and 135 fs duration. The 4PA coefficients vary from 2.6×10^{-4} to 65×10^{-4} cm^5/GW^3 in GaP, and from 3.8×10^{-4} to 9.7×10^{-4} cm^5/GW^3 in ZnTe. The anisotropy in 4PA was shown for GaP. The knowledge of the intensity-dependent 4PA coefficients is essential for the design of practical devices, such as efficient semiconductor THz sources [167,168].

8. PUBLICATION LIST

1. Publications in the topic of thesis
    - **P. S. Nugraha**, G. Krizsan, G. Polonyi, M. I. Mechler, J. Hebling, G. Toth, and J. A. Fulop, "Efficient semiconductor multicycle terahertz pulse source," J Phys B-at Mol Opt, vol. 51, 094007, 2018. [148]
    - **P. S. Nugraha**, G. Krizsán, C. Lombosi, L. Pálfalvi, G. Tóth, G. Almási, J. A. Fülöp, and J. Hebling, "Demonstration of a tilted-pulse-front pumped plane-parallel slab terahertz source," *Opt Lett*, vol. 44, pp. 1023-1026, 2019. [79]
    - B. Monoszlai, **P. S. Nugraha**, Gy. Polonyi, Gy. Tóth, L. Pálfalvi, L. Nasi, Z. Ollmann, E.J. Rohwer, G. Gaumann, T. Feurer, J. Hebling, and J. A. Fülöp, "Measurement of four-photon absorption in semiconductors," submitted to *Opt Express*, 2019.
2. Non-refereed conference abstracts in the topic of thesis
    - G. Tóth, **P. S. Nugraha**, G. Krizsán, M. I. Mechler, G. Polónyi, J. Hebling, and J. A. Fülöp, "Efficient semiconductor source of multicycle terahertz pulses using intensity-modulated pump," in *Conference on Lasers and Electro-Optics*, OSA Technical Digest (online) (Optical Society of America, 2018).
    - J. A. Fulop, **P. S. Nugraha**, L. Palfalvi, G. Krizsan, C. Lombosi, G. Toth, G. Almasi, and J. Hebling, "Demonstration of a tilted-pulse-front pumped plane-parallel slab terahertz source," *2018 43rd International Conference on Infrared, Millimeter, and Terahertz Waves (Irmmw-THz)*, 2018.
    - **P. S. Nugraha**, G. Krizsan, C. Lombosi, G. Toth, L. Palfalvi, G. Almasi, and J. Hebling, and J. A. Fulop, "Tilted-pulse-front pumped plane-parallel $LiNbO_3$ slab THz source," *2019 44th International Conference on Infrared, Millimeter, and Terahertz Waves (Irmmw-THz)*, 2019.
    - **P. S. Nugraha**, G. Krizsán, C. Lombosi, L. Pálfalvi, G. Tóth, G. Almási, J. A. Fülöp, and J. Hebling, "Demonstration of a titled-pulse-front pumped plane-parallel slab terahertz source," in 2019 Conference on Lasers and Electro-Optics Europe and European Quantum Electronics Conference, OSA Technical Digest (Optical Society of America, 2019).

- G. Polónyi, B. Monoszlai, **P. S. Nugraha,** G. Tóth, L. Pálfalvi, L. Nasi, Z. Ollmann, E. J. Rohwer, G. Gäumann, T. Feurer, J. Hebling, and J. A. Fülöp, "Measurement of effective four-photon absorption in semiconductors," in Nonlinear Optics (NLO), OSA Technical Digest (Optical Society of America, 2019) [167].
- G. Polónyi, B. Monoszlai, **P. S. Nugraha**, G. Tóth, L. Pálfalvi, L. Nasi, Z. Ollmann, E. J. Rohwer, G. Gäumann, T. Feurer, J. Hebling, and J. A. Fülöp, "Measurement of effective four-photon absorption in semiconductors," in 2019 Conference on Lasers and Electro-Optics Europe and European Quantum Electronics Conference, OSA Technical Digest (Optical Society of America, 2019)[168].

3. Publications in other topics
    - S. Li, **P. S. Nugraha**, X. Su, X. Chen, Q. Yang, M. Unferdorben, F. Kovács, S. Kunsági-Máté, M. Liu, X. Zhang, C. Ouyang, Y. Li, J. A. Fülöp, J. Han, and W. Zhang, "Terahertz electric field modulated mode coupling in graphene-metal hybrid metamaterials," *Opt Express*, vol. 27, pp. 2317-2326, 2019.

4. Non-refereed conference abstracts in other topic
    - S. Li, **P. S. Nugraha**, A. Sharma, C. Lombosi, Z. Ollmann, I. Márton, G. Farkas, J. Hebling, P. Dombi, and J. A. Fülöp, "Terahertz-induced electron emission from a gold surface," in 2019 Conference on Lasers and Electro-Optics Europe and European Quantum Electronics Conference, OSA Technical Digest (Optical Society of America, 2019).

9. ACKNOWLEDGMENT

Firstly, I would like to thank my supervisor, Dr. József András Fülöp for his guidance and the opportunities that he provided involving me in the lab work in Szentágothai Research Centre. I am especially grateful for his support and guidance for me to take and finish my PhD degree at the University of Pécs.

I would like to thank Prof. Dr. János Hebling from MTA-PTE High-Intensity Terahertz Research Group for his hospitality, receiving me into his group, as well as for his guidance and directives for experimental work. I would also like to thank Dr. Gábor Almási Head of Institute of Physic, the University of Pécs for receiving me, his guidance and help at all university activities. I would to thanks Prof. Dr. Thomas Feurer from the Institute of Physics, University of Bern, Switzerland, for his hospitality receiving us to use his laboratory and provide all necessary facilities to support our measurement. I also thank Dr. Tóth György and Dr. Polónyi Gyula for helping on the development of models and numerical tools to support the calculation and analysis in Chapter 4.2 and 4.3.

I owe special thanks for Andrea Lóki, the managing expert of the Institute of Physics who helped me through all the countless mazes of bureaucratic paperwork. I want to thanks Dr. Monoszlai Baláz, Dr. Ollman Zoltán, Shaoxian Lee, and Krizsán Gergő, who help me to do the experiment and to share much time for discussing. I am also grateful for Dr. Tibai Zoltán and those colleagues and lab mates at University of Pécs, Szentágothai Research Centre and THz group ELI-ALPS who provided me help and company during the long working hours and sometimes even after them.

Finally, I would thank my beloved parent, my wife, my children, and the whole of my big family for getting me here. I am very grateful for all of their support, encouragement, and patience that they provided me over the years of my life.

10. REFERENCES

[1] C. Fattinger and D. Grischkowsky, Appl Phys Lett **53**, 1480 (1988).

[2] W. Ghann and J. Uddin, in *Terahertz Spectroscopy - A Cutting Edge Technology*2017).

[3] S. S. Dhillon *et al.*, Journal of Physics D: Applied Physics **50**, 043001 (2017).

[4] B. B. Hu and M. C. Nuss, Opt Lett **20**, 1716 (1995).

[5] D. Mittleman, M. Gupta, R. Neelamani, R. Baraniuk, J. Rudd, and M. Koch, Applied Physics B **68**, 1085 (1999).

[6] J. A. Zeitler and L. F. Gladden, European Journal of Pharmaceutics Biopharmaceutics **71**, 2 (2009).

[7] M. Tonouchi, Nature Photonics **1**, 97 (2007).

[8] P. U. Jepsen, D. G. Cooke, and M. Koch, Laser Photonics Reviews **5**, 124 (2011).

[9] E. Brown, F. Smith, and K. McIntosh, Journal of Applied Physics **73**, 1480 (1993).

[10] S. Verghese, K. A. McIntosh, S. Calawa, W. F. Dinatale, E. K. Duerr, and K. A. Molvar, Appl Phys Lett **73**, 3824 (1998).

[11] J. Mangeney, A. Merigault, N. Zerounian, P. Crozat, K. Blary, and J. Lampin, Appl Phys Lett **91**, 241102 (2007).

[12] H. W. Hubers, S. G. Pavlov, H. Richter, A. D. Semenov, L. Mahler, A. Tredicucci, H. E. Beere, and D. A. Ritchie, Appl Phys Lett **89**, 061115 (2006).

[13] T. Göbel, D. Stanze, B. Globisch, R. J. Dietz, H. Roehle, and M. Schell, Opt Lett **38**, 4197 (2013).

[14] H. Zhang *et al.*, J Nondestruct Eval **36**, 34 (2017).

[15] M. C. Beard, G. M. Turner, and C. A. Schmuttenmaer, The Journal of Physical Chemistry B **106**, 7146 (2002).

[16] M. Hangyo, T. Nagashima, and S. Nashima, Measurement Science Technology **13**, 1727 (2002).

[17] D. N. Basov, R. D. Averitt, D. van der Marel, M. Dressel, and K. Haule, Reviews of Modern Physics **83**, 471 (2011).

[18] J. Hebling, J. Fülöp, M. Mechler, L. Pálfalvi, C. Tőke, and G. J. a. p. a. Almási, (2011).

[19] T. Meade, Y. Lee, V. Perlin, H. Winful, T. Norris, and A. Galvanauskas, in *Eleventh International Symposium on Space Terahertz Technology* (Citeseer, 2000), p. 326.

[20] Y.-S. Lee, *Principles of Terahertz Science and Technology* (Springer Publishing Company, Incorporated, 2008).

[21] F. Zernike and P. R. Berman, Phys Rev Lett **15**, 999 (1965).

[22] K. H. Yang, J. R. Morris, P. L. Richards, and Y. R. Shen, Appl Phys Lett **23**, 669 (1973).

[23] G. D. Boyd, T. J. Bridges, C. K. N. Patel, and E. Buehler, Appl Phys Lett **21**, 553 (1972).

[24] W. Shi, Y. J. Ding, and P. G. Schunemann, Opt Commun **233**, 183 (2004).

[25] W. Shi, Y. J. Ding, N. Fernelius, and K. Vodopyanov, Opt Lett **27**, 1454 (2002).

[26] B. Lax, R. L. Aggarwal, and G. Favrot, Appl Phys Lett **23**, 679 (1973).

[27] S. Y. Tochitsky, C. Sung, S. E. Trubnick, C. Joshi, and K. L. Vodopyanov, J. Opt. Soc. Am. B **24**, 2509 (2007).

[28] T. Tanabe, K. Suto, J. Nishizawa, K. Saito, and T. Kimura, Appl Phys Lett **83**, 237 (2003).

[29] T. Taniuchi and H. Nakanishi, Electronics Letters **40**, 327 (2004).

[30] K. Kawase, M. Sato, T. Taniuchi, and H. Ito, Appl Phys Lett **68**, 2483 (1996).

[31] T. J. Edwards, D. Walsh, M. B. Spurr, C. F. Rae, M. H. Dunn, and P. G. Browne, Opt Express **14**, 1582 (2006).

[32] T. Yajima and N. Takeuchi, Japanese Journal of Applied Physics **9**, 1361 (1970).

[33] K. H. Yang, P. L. Richards, and Y. R. Shen, Appl Phys Lett **19**, 320 (1971).

[34] L. Xu, X. C. Zhang, and D. H. Auston, Appl Phys Lett **61**, 1784 (1992).

[35] B. Ferguson and X.-C. Zhang, Nature Materials **1**, 26 (2002).

[36] A. Rice, Y. Jin, X. F. Ma, X. C. Zhang, D. Bliss, J. Larkin, and M. Alexander, Appl Phys Lett **64**, 1324 (1994).

[37] M. Nagai, K. Tanaka, H. Ohtake, T. Bessho, T. Sugiura, T. Hirosumi, and M. Yoshida, Appl Phys Lett **85**, 3974 (2004).

[38] G. Chang, C. J. Divin, C. H. Liu, S. L. Williamson, A. Galvanauskas, and T. B. Norris, Opt Express **14**, 7909 (2006).

[39] P. H. Siegel, IEEE Transactions on Microwave Theory and Techniques **50**, 910 (2002).

[40] K. L. Vodopyanov, Laser Phys **19**, 305 (2009).

[41] J. Hebling, K. L. Yeh, M. C. Hoffmann, B. Bartal, and K. A. Nelson, J Opt Soc Am B **25**, B6 (2008).

[42] W. D. Johnston and I. P. Kaminow, Physical Review **188**, 1209 (1969).

[43] A. Nahata, A. S. Weling, and T. F. Heinz, Appl Phys Lett **69**, 2321 (1996).

[44] R. S. Weis and T. K. Gaylord, Appl Phys a-Mater **37**, 191 (1985).

[45] A. Kling, J. G. Marques, J. G. Correia, M. F. da Silva, E. Diéguez, F. Agulló-López, and J. C. Soares, Nuclear Instruments and Methods in Physics Research Section B: Beam Interactions with Materials and Atoms **113**, 293 (1996).

[46] K. Kitamura, Y. Furukawa, Y. Ji, M. Zgonik, C. Medrano, G. Montemezzani, and P. Günter, Journal of Applied Physics **82**, 1006 (1997).

[47] Y. Furukawa, K. Kitamura, S. Takekawa, A. Miyamoto, M. Terao, and N. Suda, Appl Phys Lett **77**, 2494 (2000).

[48] M. Nakamura, S. Higuchi, S. Takekawa, K. Terabe, Y. Furukawa, and K. Kitamura, Japanese Journal of Applied Physics **41**, L49 (2002).

[49] T. Fujiwara, M. Takahashi, M. Ohama, A. Ikushima, Y. Furukawa, and K. J. E. l. Kitamura, **35**, 499 (1999).

[50] D. A. Bryan, R. Gerson, and H. E. Tomaschke, Appl Phys Lett **44**, 847 (1984).

[51] Y. Furukawa, K. Kitamura, S. Takekawa, K. Niwa, and H. Hatano, Opt Lett **23**, 1892 (1998).

[52] T. R. Volk, N. M. Rubinina, V. I. Pryalkin, V. V. Krasnikov, and V. V. Volkov, Ferroelectrics **109**, 345 (1990).

[53] L. Palfalvi, J. Hebling, G. Almasi, A. Peter, K. Polgar, K. Lengyel, and R. Szipocs, Journal of Applied Physics **95**, 902 (2004).

[54] M. Aillerie, P. Bourson, M. Mostefa, F. Abdi, and M. D. Fontana, Journal of Physics: Conference Series **416**, 012002 (2013).

[55] D. H. Jundt, Opt Lett **22**, 1553 (1997).

[56] O. Gayer, Z. Sacks, E. Galun, and A. Arie, Applied Physics B **91**, 343 (2008).

[57] L. Palfalvi, J. Hebling, J. Kuhl, A. Peter, and K. Polgar, Journal of Applied Physics **97**, 123505 (2005).

[58] J. Hebling, G. Almasi, I. Kozma, and J. Kuhl, Opt Express **10**, 1161 (2002).

[59] J. Hebling, Optical and Quantum Electronics **28**, 1759 (1996).

[60] J. A. Fulop, L. Palfalvi, G. Almasi, and J. Hebling, Opt Express **18**, 12311 (2010).

[61] A. G. Stepanov, J. Kuhl, I. Z. Kozma, E. Riedle, G. Almási, and J. Hebling, Opt Express **13**, 5762 (2005).

[62] J. A. Fulop, L. Palfalvi, M. C. Hoffmann, and J. Hebling, Opt Express **19**, 15090 (2011).

[63] K. Ravi, W. R. Huang, S. Carbajo, X. J. Wu, and F. Kartner, Opt Express **22**, 20239 (2014).

[64] L. Palfalvi, J. A. Fulop, G. Almasi, and J. Hebling, Appl Phys Lett **92** (2008).

[65] Z. Ollmann, J. Hebling, and G. Almasi, Appl Phys B-Lasers O **108**, 821 (2012).

[66] L. Pálfalvi, Z. Ollmann, L. Tokodi, and J. Hebling, Opt Express **24**, 8156 (2016).

[67] B. K. Ofori-Okai, P. Sivarajah, W. Ronny Huang, and K. A. Nelson, Opt. Express **24**, 5057 (2016).

[68] K. Murate, M. J. Roshtkhari, X. Ropagnol, and F. Blanchard, Opt Lett **43**, 2090 (2018).

[69] L. Pálfalvi, G. Tóth, L. Tokodi, Z. Márton, J. A. Fülöp, G. Almási, and J. Hebling, Opt Express **25**, 29560 (2017).

[70] X. C. Zhang, B. B. Hu, J. T. Darrow, and D. H. Auston, Appl Phys Lett **56**, 1011 (1990).

[71] S. L. Chuang, S. Schmitt-Rink, B. I. Greene, P. N. Saeta, and A. F. Levi, Phys Rev Lett **68**, 102 (1992).

[72] Y. H. Jin and X. C. Zhang, Journal of Nonlinear Optical Physics & Materials **04**, 459 (1995).

[73] M. Reid and R. Fedosejevs, Appl Opt **44**, 149 (2005).

[74] X. C. Zhang, Y. Jin, and X. F. Ma, Appl Phys Lett **61**, 2764 (1992).

[75] Q. Chen, M. Tani, Z. Jiang, and X. C. Zhang, J. Opt. Soc. Am. B **18**, 823 (2001).

[76] R. W. Boyd, *Nonlinear Optics, Third Edition* (Academic Press, Inc., 2008).

[77] X. Xie, J. Xu, and X. C. Zhang, Opt Lett **31**, 978 (2006).

[78] W. M. Haynes, *CRC handbook of chemistry and physics, 97th Edition* (CRC Press LLC Taylor & Francis Group, Boca Raton; Florence, 2017), p.^pp. 2159.

[79] F. Blanchard *et al.*, Opt Express **15**, 13212 (2007).

[80] T. Löffler, T. Hahn, M. Thomson, F. Jacob, and H. G. Roskos, Opt Express **13**, 5353 (2005).

[81] S. M. Harrel, R. L. Milot, J. M. Schleicher, and C. A. Schmuttenmaer, Journal of Applied Physics **107**, 033526 (2010).

[82] S. Vidal, J. Degert, M. Tondusson, J. Oberlé, and E. Freysz, Appl Phys Lett **98**, 191103 (2011).

[83] S. A. Ku, C. M. Tu, W. C. Chu, C. W. Luo, K. H. Wu, A. Yabushita, C. C. Chi, and T. Kobayashi, Opt Express **21**, 13930 (2013).

[84] W. L. Bond, Journal of Applied Physics **36**, 1674 (1965).

[85] A. Borghiesi and G. Guizzetti, (1991).

[86] W. Qi and Z. Xi-Cheng, Ieee J Sel Top Quant **2**, 693 (1996).

[87] X. Jia, G. Björn, H. Christina, L. Nikolai, B. Thomas, K. Nicholas, and P. Ioachim, Journal of Physics B: Atomic, Molecular and Optical Physics **51**, 154002 (2018).

[88] J. Li *et al.*, Appl Phys Lett **104**, 031117 (2014).

[89] G. Polonyi *et al.*, Opt Express **24**, 23872 (2016).

[90] F. Blanchard, B. E. Schmidt, X. Ropagnol, N. Thire, T. Ozaki, R. Morandotti, D. G. Cooke, and F. Legare, Appl Phys Lett **105**, 241106 (2014).

[91] D. Nicoletti and A. Cavalleri, Adv. Opt. Photon. **8**, 401 (2016).

[92] E. A. Nanni, W. R. Huang, K.-H. Hong, K. Ravi, A. Fallahi, G. Moriena, R. J. Dwayne Miller, and F. X. Kärtner, Nature Communications **6**, 8486 (2015).

[93] L. Pálfalvi, J. A. Fülöp, G. Tóth, and J. Hebling, Physical Review Special Topics - Accelerators and Beams **17**, 031301 (2014).

[94] A. Sharma, Z. Tibai, and J. Hebling, Phys Plasmas **23**, 063111 (2016).

[95] T. Plettner, P. P. Lu, and R. L. Byer, Physical Review Special Topics - Accelerators and Beams **9**, 111301 (2006).

[96] F. X. Kärtner *et al.*, Nuclear Instruments and Methods in Physics Research Section A: Accelerators, Spectrometers, Detectors and Associated Equipment **829**, 24 (2016).

[97] J. Lu, H. Y. Hwang, X. Li, S.-H. Lee, O. P. Kwon, and K. A. Nelson, Opt Express **23**, 22723 (2015).

[98] Z. Chen, X. B. Zhou, C. A. Werley, and K. A. Nelson, Appl Phys Lett **99**, 071102 (2011).

[99] K. H. Lin, C. A. Werley, and K. A. Nelson, Appl Phys Lett **95**, 103304 (2009).

[100] Y. S. Lee, T. Meade, V. Perlin, H. Winful, T. B. Norris, and A. Galvanauskas, Appl Phys Lett **76**, 2505 (2000).

[101] S. Carbajo, J. Schulte, X. Wu, K. Ravi, D. N. Schimpf, and F. X. Kartner, Opt Lett **40**, 5762 (2015).

[102] Y. S. Lee, T. Meade, M. DeCamp, T. B. Norris, and A. Galvanauskas, Appl Phys Lett **77**, 1244 (2000).

[103] F. D. J. Brunner, S.-H. Lee, O. P. Kwon, and T. Feurer, Opt. Mater. Express **4**, 1586 (2014).

[104] G. Toth, J. A. Fulop, and J. Hebling, Opt Express **25**, 28258 (2017).

[105] F. Blanchard, B. E. Schmidt, X. Ropagnol, N. Thiré, T. Ozaki, R. Morandotti, D. G. Cooke, and F. Légaré, Applied Physics Letters **105**, 241106 (2014).

[106] J. A. Fülöp, G. Polónyi, B. Monoszlai, G. Andriukaitis, T. Balciunas, A. Pugzlys, G. Arthur, A. Baltuska, and J. Hebling, Optica **3**, 1075 (2016).

[107] G. Polónyi *et al.*, Opt. Express **24**, 23872 (2016).

[108] G. Polónyi, M. I. Mechler, J. Hebling, and J. A. Fülöp, Ieee J Sel Top Quant **23**, 1 (2017).

[109] Y.-S. Lee, W. C. Hurlbut, K. L. Vodopyanov, M. M. Fejer, and V. G. Kozlov, Appl Phys Lett **89**, 181104 (2006).

[110] B. B. Hu, J. T. Darrow, X. C. Zhang, D. H. Auston, and P. R. Smith, Appl Phys Lett **56**, 886 (1990).

[111] S. E. Ralph and D. Grischkowsky, Appl Phys Lett **60**, 1070 (1992).

[112] J. Valdmanis and G. Mourou, IEEE Journal of Quantum Electronics **22**, 69 (1986).

[113] Q. Wu and X. C. Zhang, Appl Phys Lett **67**, 3523 (1995).

[114] P. C. M. Planken, H.-K. Nienhuys, H. J. Bakker, and T. Wenckebach, J. Opt. Soc. Am. B **18**, 313 (2001).

[115] Q. Wu and X. C. Zhang, Appl Phys Lett **68**, 1604 (1996).

[116] Q. Wu and X. C. Zhang, Appl Phys Lett **70**, 1784 (1997).

[117] M. Sheik-bahae, A. A. Said, and E. W. Van Stryland, Opt Lett **14**, 955 (1989).

[118] E. W. V. Stryland and M. Sheik-Bahae, *Z-scan technique for nonlinear materials characterization* (SPIE, 1997), Vol. 10291, Optical Science, Engineering and Instrumentation '97, p.^pp. OP.

[119] M. Sheik-Bahae, A. A. Said, T. Wei, D. J. Hagan, and E. W. V. Stryland, IEEE Journal of Quantum Electronics **26**, 760 (1990).

[120] R. Domínguez-Cruz, M. Milan, D. Vargas-Requena, A. Valencia-Rodríguez, G. Romero-Galván, M. Panduro, T. Reynosa, and M. R. Ramos-García, 2005).

[121] J. A. Hermann, Journal of Nonlinear Optical Physics & Materials **01**, 541 (1992).

[122] P. B. Chapple, J. Staromlynska, J. A. Hermann, T. J. Mckay, and R. G. Mcduff, Journal of Nonlinear Optical Physics & Materials **06**, 251 (1997).

[123] M. R. Ferdinandus, M. Reichert, T. R. Ensley, H. Hu, D. A. Fishman, S. Webster, D. J. Hagan, and E. W. Van Stryland, Opt. Mater. Express **2**, 1776 (2012).

[124] V. Y. Fedorov and S. Tzortzakis, Physical Review A **97**, 063842 (2018).

[125] D. Jain and O. Bang, in *CLEO Pacific Rim Conference 2018* (Optical Society of America, Hong Kong, 2018), p. Th3D.5.

[126] M. C. Hoffmann, K.-L. Yeh, J. Hebling, and K. A. Nelson, Opt Express **15**, 11706 (2007).

[127] M. Hohenleutner, F. Langer, O. Schubert, M. Knorr, U. Huttner, S. W. Koch, M. Kira, and R. Huber, Nature **523**, 572 (2015).

[128] B. S. Wherrett, J. Opt. Soc. Am. B **1**, 67 (1984).

[129] V. Nathan, A. H. Guenther, and S. S. Mitra, J. Opt. Soc. Am. B **2**, 294 (1985).

[130] S. J. Bepko, Phys Rev B **12**, 669 (1975).

[131] R. DeSalvo, M. Sheik-Bahae, A. A. Said, D. J. Hagan, and E. W. Van Stryland, Opt Lett **18**, 194 (1993).

[132] W. C. Hurlbut, Y.-S. Lee, K. L. Vodopyanov, P. S. Kuo, and M. M. Fejer, Opt Lett **32**, 668 (2007).

[133] T. D. Krauss, J. K. Ranka, F. W. Wise, and A. L. Gaeta, Opt Lett **20**, 1110 (1995).

[134] J. Yumoto and K. Otsuka, Physical Review Letters **54**, 1806 (1985).

[135] I. B. Zotova and Y. J. Ding, Appl. Opt. **40**, 6654 (2001).

[136] C. M. Cirloganu, P. D. Olszak, L. A. Padilha, S. Webster, D. J. Hagan, and E. W. V. Stryland, Opt Lett **33**, 2626 (2008).

[137] D. Peceli *et al.*, in *Nonlinear Optics* (Optical Society of America, Kohala Coast, Hawaii, 2013), p. NTu1B.6.

[138] B.-U. Sohn, M. Kang, J. W. Choi, A. M. Agarwal, K. Richardson, and D. T. H. Tan, APL Photonics **4**, 036102 (2019).

[139] P. S. Nugraha, G. Krizsán, G. Polónyi, M. I. Mechler, J. Hebling, G. Tóth, and J. A. Fülöp, Journal of Physics B: Atomic, Molecular and Optical Physics **51**, 094007 (2018).

[140] K. L. Vodopyanov, M. M. Fejer, X. Yu, J. S. Harris, Y. S. Lee, W. C. Hurlbut, V. G. Kozlov, D. Bliss, and C. Lynch, Appl Phys Lett **89**, 141119 (2006).

[141] G. Tóth, L. Pálfalvi, J. A. Fülöp, G. Krizsán, N. H. Matlis, G. Almási, and J. Hebling, Opt Express **27**, 7762 (2019).

[142] G. Tóth, L. Pálfalvi, Z. Tibai, L. Tokodi, J. A. Fülöp, Z. Márton, G. Almási, and J. Hebling, Opt Express **27**, 30681 (2019).

[143] J. A. Fülöp and J. Hebling, in *Recent optical and photonic technologies*, edited by K. Y. Kim (InTech, Rijeka, 2010), p. Ch. 11.

[144] S. W. Huang, E. Granados, W. R. Huang, K. H. Hong, L. E. Zapata, and F. X. Kartner, Opt Lett **38**, 796 (2013).

[145] J. A. Fulop, Z. Ollmann, C. Lombosi, C. Skrobol, S. Klingebiel, L. Palfalvi, F. Krausz, S. Karsch, and J. Hebling, Opt Express **22**, 20155 (2014).

[146] Z. Tibai, M. Unferdorben, S. Turnar, A. Sharma, J. A. Fulop, G. Almasi, and J. Hebling, J Phys B-at Mol Opt **51** (2018).

[147] K. Ravi, W. R. Huang, S. Carbajo, E. A. Nanni, D. N. Schimpf, E. P. Ippen, and F. X. Kärtner, Opt Express **23**, 5253 (2015).

[148] C. Somma, K. Reimann, C. Flytzanis, T. Elsaesser, and M. Woerner, Phys Rev Lett **112**, 146602 (2014).

[149] P. S. Nugraha, G. Krizsán, C. Lombosi, L. Pálfalvi, G. Tóth, G. Almási, J. A. Fülöp, and J. Hebling, Opt Lett **44**, 1023 (2019).

[150] A. Leitenstorfer, S. Hunsche, J. Shah, M. C. Nuss, and W. H. Knox, Applied Physics Letters **74**, 1516 (1999).

[151] E. D. Palik, *Handbook of optical constants of solids* (Academic Press, Orlando, 1985), Academic Press handbook series.

[152] B. Bartal, I. Z. Kozma, A. G. Stepanov, G. Almási, J. Kuhl, E. Riedle, and J. Hebling, Applied Physics B **86**, 419 (2007).

[153] D. F. Nelson and E. H. Turner, Journal of Applied Physics **39**, 3337 (1968).

[154] P. Y. Yu and M. Cardona, *Fundamentals of semiconductors: physics and materials properties* (Springer, 2010).

[155] G. Tóth, J. A. Fülöp, and J. Hebling, Opt. Express **25**, 28258 (2017).

[156] K. Wynne and J. J. Carey, Optics Communications **256**, 400 (2005).

[157] T. Tanabe, K. Suto, J. Nishizawa, K. Saito, and T. Kimura, Applied Physics Letters **83**, 237 (2003).

[158] F. Liu, Y. F. Li, Q. R. Xing, L. Chai, M. L. Hu, C. L. Wang, Y. Q. Deng, Q. Sun, and C. Y. Wang, J Optics-Uk **12**, 095201 (2010).

[159] Y. Li, F. Liu, Y. Li, L. Chai, Q. Xing, M. Hu, and C. Wang, Appl. Opt. **50**, 1958 (2011).

[160] Y. Yin, J. Li, X. Ren, Y. Wang, A. Chew, and Z. Chang, Opt Express **24**, 24989 (2016).

[161] M. Yin, H. P. Li, S. H. Tang, and W. Ji, Applied Physics B **70**, 587 (2000).

[162] M. Schultze *et al.*, Science **346**, 1348 (2014).

[163] A. A. Said, M. Sheik-Bahae, D. J. Hagan, T. H. Wei, J. Wang, J. Young, and E. W. Van Stryland, J. Opt. Soc. Am. B **9**, 405 (1992).

[164] R. L. Sutherland, D. G. McLean, and S. Kirkpatrick, *Handbook of nonlinear optics* (Marcel Dekker, New York, 2003), 2nd edn., Optical engineering, 82.

[165] V. I. Zavelishko, V. A. Martynov, S. M. Saltiel, and V. G. Tunkin, Soviet Journal of Quantum Electronics **5**, 1392 (1975).

[166] S. V. Popov, Y. P. Svirko, and N. I. Zheludev, *Susceptibilty tensors for nonlinear optics* (IOP Publishing Ltd., 1995).

[167] G. Polónyi *et al.*, in *Nonlinear Optics (NLO)* (Optical Society of America, Waikoloa Beach, Hawaii, 2019), p. NTu4A.41.

[168] G. Polónyi *et al.*, in *2019 Conference on Lasers and Electro-Optics Europe and European Quantum Electronics Conference* (Optical Society of America, Munich, 2019), p. ce_p_32.

[169] T. Kampfrath, K. Tanaka, and K. A. Nelson, Nature Photonics **7**, 680 (2013).

[170] J. Hebling, G. Almási, I. Z. Kozma, and J. Kuhl, Opt. Express **10**, 1161 (2002).

[171] J. A. Fülöp, Z. Ollmann, C. Lombosi, C. Skrobol, S. Klingebiel, L. Pálfalvi, F. Krausz, S. Karsch, and J. Hebling, Opt. Express **22**, 20155 (2014).